

A tutorial on the 3ω method for measuring thermal conductivity from macro to micro dimensions

Cite as: J. Appl. Phys. 138, 211101 (2025); doi: 10.1063/5.0299596

Submitted: 28 August 2025 · Accepted: 13 November 2025 ·

Published Online: 5 December 2025



View Online



Export Citation



CrossMark

Xiao Yang,^{1,2,3} Haibo Zhao,^{1,4} Chunyang Wang,^{1,3} Yanan Shen,^{1,4} Zewen Song,^{1,4} Haisheng Chen,^{1,2,3,4,a} Ting Zhang,^{1,2,3,4,5,a} and Xinghua Zheng^{1,3,4,a}

AFFILIATIONS

¹Institute of Engineering Thermophysics, Chinese Academy of Sciences, Beijing 100190, China

²Nanjing Institute of Future Energy System, Nanjing 211135, China

³Key Laboratory of Long-Duration and Large-Scale Energy Storage, Chinese Academy of Sciences, Beijing 100190, China

⁴University of Chinese Academy of Sciences, Beijing 100049, China

⁵University of Chinese Academy of Sciences, Nanjing 211135, China

^aAuthors to whom correspondence should be addressed: chen_hs@iet.cn; zhangting@iet.cn; and zhengxh@iet.cn

ABSTRACT

The 3ω harmonic detection method has been widely applied to develop the thermal functional materials and for the fabrication of devices in fields such as aerospace and energy conservation. It is adaptable for measuring the thermal conductivity of materials with various geometries, ranging from macroscopic to micro- and nanoscale, in both in-plane and out-of-plane directions. This tutorial introduces the measurement principles of the 3ω method and highlights important considerations for its application to different materials.

© 2025 Author(s). All article content, except where otherwise noted, is licensed under a Creative Commons Attribution (CC BY) license (<https://creativecommons.org/licenses/by/4.0/>). <https://doi.org/10.1063/5.0299596>

06 December 2025 08:34:26

I. INTRODUCTION

Since Cahill *et al.* proposed the 3ω method, through the unremitting efforts by researchers worldwide, this method has achieved precise measurements of thermal conductivity in various materials ranging from macroscopic to nanoscale, including bulk, fluids (gases and liquids), porous media, powders, axial fibers, in-plane sheets, as well as in-plane and out-of-plane films. Multi-parameter measurements of thermal conductivity, specific heat capacity, heat storage coefficient, thermal contact resistance, and thermal diffusivity have been achieved. It is currently the thermal property measurement method with the most types of measurable materials, the widest measurable scale, and the most measurable parameters. To overcome the disadvantages of the traditional 3ω method, such as electrode portability and easy breakage of single metal electrodes for measuring fluids and powders, the Institute of Engineering Thermophysics, Chinese Academy of Sciences (IET) has developed an independent detector based on

polyimide and sapphire substrates.¹ Germany's Linseis has developed a thin-film physical property instrument for measuring the thermal conductivity, electrical conductivity, and Seebeck coefficient of thin films. The IET has also independently developed a multi-dimensional and cross-scale *in situ* measurement instrument for the thermoelectric properties of materials, which makes this method go beyond the laboratory and enter the market and commercial application. A comparison of the 3ω method with other methods is presented in Table I.^{2–12} Compared to alternative methods, the 3ω method demonstrates distinct advantages in sample preparation, testing methodology, and measurement precision, thereby generating considerable scholarly interest in its investigation. This tutorial will provide a detailed introduction to the thermal conductivity measurement principle, model, and experimental precautions of this method for different scales and types of materials, to meet the needs of graduate students and researchers in related fields.

TABLE I. Comparisons of each method in the actual measurement.

Performance	Methods		
	Photothermal reflectance method	Raman method	TDTR
Preparation	Easy	Easy	Easy
Measurement	Simple	Simple	Complex
Sample quality	Yes	Yes	Yes
Sample damage	No	No	Yes
Temperature (K)	270–670 ²	80–670 ⁴	120–1270 ⁵
Error (%)	8 ³	8 ⁴	5 ⁶
Performance	Methods		
	T-type method	Micro-device method	3 ω method
Preparation	Difficult	Difficult	Easy
Measurement	Simple	Complex	Simple
Sample quality	No	No	No
Sample damage	Yes	Yes	Yes
Temperature (K)	80–400 ⁷	10–770 ⁹	30–750 ¹⁰
Error (%)	5 ⁸	5 ⁹	5 ¹¹

II. DEVELOPMENT OF THE 3 ω METHOD

A. Traditional 3 ω method

1. Solid and anisotropic materials

The 3 ω harmonic detection method is widely used in the thermal characterization of solid isotropic and anisotropic materials, such as anisotropic carbon nanotube arrays, silicon carbide crystals, and composite materials. For solid materials, it is necessary to prepare a micro-heating detector of a certain scale and shape on the surface of the tested material, which can be used as both a heater and a temperature sensor. The thermal conductivity of the tested material is then determined from the frequency relationship between temperature changes and thermal wave fluctuations. During the experiment, a periodic alternating current with an angular frequency of 1 ω was applied to the metal film, denoted as $I = I_0 \cos(\omega t)$, as shown in Fig. 1. Due to the certain resistance of

the metal film, the periodic heat generated by the Joule effect will heat the metal film and material at a frequency of 2 ω . After absorbing the heat, the metal film and tested material will generate a temperature wave with a frequency of 2 ω called $\Delta T = \Delta T_0 \cos(2\omega t + \phi)$. For pure metals used as temperature sensors, the increase in temperature causes an increase in resistance, and the frequency of change in the increased resistance is also 2 ω . The increased resistance works together with an alternating current with a frequency of 1 ω to produce a secondary voltage with a frequency of 3 ω . Considering the heating frequency of the heater, the amplitude and phase angle ϕ of the voltage signal are related to the shape and thermal properties of the heater, as well as the thermal properties of the tested material. According to Ohm's law, a simple derivation is as follows:

$$R = R_0(1 + \alpha_R \Delta T), \quad \alpha_R = 1/R(dR/dT), \quad (1)$$

$$U_\omega + U_{3\omega} = R_0 I_0 \cos \omega t + R_0 I_0 \alpha_R \Delta T_0 \cos(2\omega t + \phi)/2 \\ + R_0 I_0 \alpha_R \Delta T_0 \cos(3\omega t + \phi)/2, \quad (2)$$

where R_0 is the resistance, α_R is the temperature coefficient of resistance, U_ω and $U_{3\omega}$ are the ω and 3 ω voltage amplitude, respectively. During the experiment, the directly measurable signals were the third harmonic voltage and fundamental voltage, rather than temperature fluctuation signals. In theory, the thermal conductivity of the sample material can be determined by the real or imaginary part of the third harmonic. However, in the experimental process, due to the small imaginary component of the third harmonic, it is difficult to detect its accurate signal using a lock-in amplifier in certain frequency bands. Generally, the effective value of the real part or amplitude of the third harmonic is used to calculate the real part or amplitude of the temperature wave amplitude of the micro-heating detector ($T_{2\omega} = 2U_{3\omega}/\alpha_R U_\omega$). Since the specific heat capacity, thermal conductivity, and heating frequency of the material are independent of the scale of the micro-heating detector, the thermal conductivity of the material with an infinitely narrow micro-heating detector on a semi-infinite volume surface can be determined based on the relationship between detector temperature fluctuations and frequency changes ($d\Delta T/d\ln\omega = -P/2\pi\lambda l^2$), where λ is the thermal conductivity of the semi-infinite volume, P/l is the power amplitude of per unit length generated in a 2 ω line heat source.

The 3 ω method is a transient measurement method that can effectively reduce the influence of thermal flux and maintain a stable heat flux density, thereby improving both testing speed and accuracy. The 3 ω method uses a small sample size and effectively reduces radiation errors by reducing the heat transfer area. The steady-state method requires a long equilibrium time, whereas the 3 ω method can be completed in a matter of seconds, increasing testing speed. For anisotropic materials, the flash method can only obtain the thermal properties of anisotropic materials along a single direction by directly obtaining thermal diffusivity. The density and specific heat of the sample must be measured again to derive and calculate thermal conductivity. Therefore, the error introduced by multiple measurements also increases, and the flash method cannot directly test transparent materials.

By using the 3 ω method to measure the thermal conductivity of isotropic solid materials, micro-heating detectors can be directly

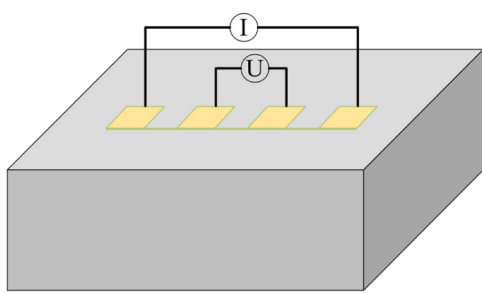


FIG. 1. Micro detector of the 3 ω method.

deposited on their surfaces. However, for conductive samples, an insulating layer needs to be deposited on their surface firstly, and then a micro-metal-heating film is deposited on the surface of the insulation layer for measurement. This requires the surface of the sample material to be as smooth and flat as possible to facilitate the arrangement of the detector. The thickness of the sample can range from hundreds of nanometers to a few millimeters. Experimental proof has shown that micro-heating detectors with a width of tens of micrometers can be deposited on the surface of the tested material with a gap of hundreds of nanometers. This method can produce highly accurate measurement results. In addition, the surface smoothness of the tested sample also affects the adhesion of the micro-heating detector.

The selection of metal material, manufacturing process, and detector size for the micro-heating detector on the surface of the tested sample have a significant impact on the measurement structure of the method. Usually, researchers choose metal materials with a good linear relationship between resistance and temperature as micro-heating detectors. At temperatures below room temperature, silver is often used as a micro-heating detector. However, silver has poor adhesion to the surface of the tested sample. Metal nickel (Ni) or titanium (Ti) with a thickness of several to tens of nanometers can be deposited as a transition layer first, and then a certain thickness of silver can be deposited as a micro-metal heater. At temperatures above room temperature, platinum (Pt) or gold (Au) is often selected as the material for micro-heating detectors. Ultimately, it is necessary to ensure that the resistivity of the selected metal is moderate, and the resistance of the micro-heating detector at typical scales should be maintained at several to tens of ohms.

The experimental system includes lock-in amplifier, signal generator, operational amplifier, adjustable resistance box, and vacuum temperature control furnace, which is shown in Fig. 2. Compared with traditional measurement techniques, the 3ω

method has little or even negligible influence from thermal radiation, and the testing time is very short. Usually, it takes a few seconds to measure the third harmonic voltage signal and fundamental voltage at a certain heating frequency, and then calculate the temperature fluctuation caused by the micro-heating detector at that frequency. Placing the sample in a vacuum chamber and maintaining a certain degree of vacuum can eliminate the influence of natural convection heat transfer of air and effectively shield external interference signals. When the third harmonic voltage is measured at both ends of a micro-heating detector at a given temperature and frequency, a reasonable fundamental voltage should be selected first, and the third harmonic voltage should be as close as possible to $1/1000$ – $1/500$ of the fundamental voltage. At this point, the reliability of the measurement results is relatively high.¹³

To test bulk materials, a set of micro-detectors must be deposited on the material's surface. The metal film is used as both a heater and a temperature sensor. The thermal conductivity of the tested material is then calculated based on the relationship between the frequency of thermal waves and temperature changes. The tested sample is generally a non-conductive solid, and for conductive solids, a layer of insulating film should be deposited on the surface first. The thickness of the insulating layer influences the error generated by thermal diffusion effects. If the layer is thinner, the resulting error will be smaller. If Cahill's slope- 3ω method is used to measure the thermal conductivity of a thin film deposited on the substrate surface, it is required that the thickness of the film must be greater than five times the half-width of the metal-heating film to satisfy the assumption that the sample satisfies semi-infinite size at low frequencies. For the measurement of thermal conductivity of film-substrate structures, if the thermal parameters of the substrate are known and its thermal conductivity is much higher than that of the thin film, the diffusion- 3ω method can currently be used to measure the thermal conductivity of thin films with a thickness greater than 20–50 nm. The thermal conductivity of thin films with a thickness of several hundred nanometers can be directly measured at high frequencies. To ensure good continuity of the metal-heating film, the surface of the sample should be as smooth as possible. Generally, the sample is first placed in acetone and sonicated for at least one hour, then washed in isopropanol and distilled water, dried, and then prepared as a heating film. If the surface roughness of the sample is relatively large, it can also be polished with alumina powder with a particle diameter of about $1\text{ }\mu\text{m}$ first, and then cleaned as described above. The standard for testing whether the adhesion strength of the metal-heating film can meet the requirements is to hang the sample with the electrode lead holding the heating film, and ensure that the heating film on the surface does not fall off. The heating film mask is shown in Fig. 3. Yamane *et al.*¹⁴ used sputtering, spraying, evaporation, and chemical deposition methods to process SiO_2 thin films with thicknesses of 100, 500, and 1000 nm on the surface of a 0.5 mm Si substrate. Aluminum or copper heating films with a width of $8\text{ }\mu\text{m}$, a length of 1.4 mm, and a thickness of 300 nm were processed using microfilament printing technology. The out-of-plane thermal conductivity of SiO_2 films produced by different processes was tested using the 3ω method.

For measuring the thermal conductivity of anisotropic materials, multiple sets of micro-detectors need to be deposited on the

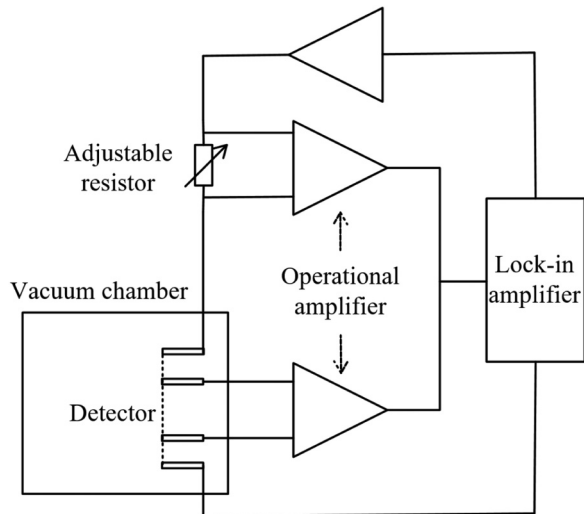


FIG. 2. 3ω experimental testing system.

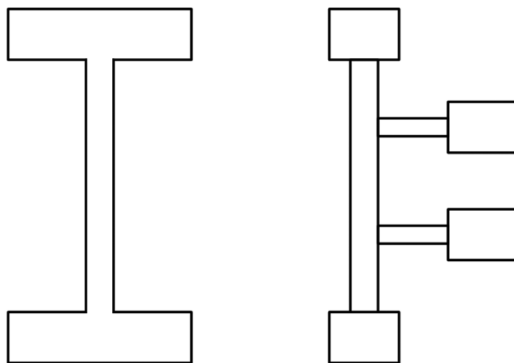


FIG. 3. Two-pad and four-pad heater.

material surface. The combination of the width of the micro-heating detector and the thickness of the tested sample determines the measurement sensitivity of the thermophysical properties of the sample in the out-of-plane and in-plane directions. When the width of the micro-heating detector is wide or relatively large compared to the thickness of the sample, it can be considered as a surface heat source, and the heat is transferred one-dimensional along the thickness direction of the sample. The measured temperature fluctuations should be considered sensitive to the thermal conductivity perpendicular to the surface direction of the sample (i.e., the out-of-plane direction of the sample). If the line width of the micro-heating detector is narrow or very small compared to the thickness of the sample, it can be considered as a line heat source. The heat generated in the micro-heating detector is not only transferred along the thickness direction, but also laterally transferred inside the tested sample. The measured temperature signal will be affected by the thermal conductivity parallel to the direction of the sample (in-plane) and perpendicular to the direction of the sample surface (out-of-plane). The heat transfer characteristics inside the sample are shown in Figs. 4 and 5. For the semi-infinite solid model of a single-layer film with a substrate, Carslaw and Jaeger¹⁵ provided the equation solution for temperature fluctuations. Borca-Tasciuc *et al.*¹⁶ provided a simplified formula for temperature rise. For the semi-infinite solid model of multilayer films with substrates, Borca-Tasciuc *et al.* provided a general solution for the two-dimensional thermal conductivity model of the multilayer film and substrate system. Su *et al.*¹⁷ provided a temperature rise formula for the multi-layer system and measured the thermal conductivity of 6H-SiC crystals in the x , y , and z directions using

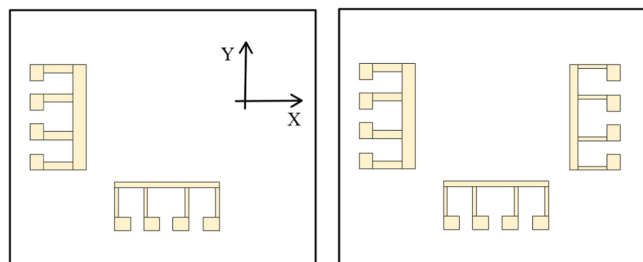


FIG. 5. Structure of a micro-heating detector for measuring the thermal conductivity of anisotropic materials.

multiple detectors. Sources of error in testing anisotropic materials stem partly from detector preparation, where appropriate length and width dimensions reduce measurement discrepancies in thermal conductivity across different orientations. Furthermore, excessive variations in isotropic thermal conductivity may also lead to testing inaccuracies. At this stage, it is possible to utilize the differences in sensitivity across various frequency bands of the 3ω signal to decouple anisotropic thermal conductivity.

Borca-Tasciuc *et al.*¹⁶ simultaneously measured the thermal conductivity of anisotropic superlattice thin films in the temperature range of 80–300 K using a differential two-wire method. Two parallel micro-heating detectors with widths of 2 and 30 μm were used. Its research has shown that a 2- μm micro-heating detector is highly sensitive to the out-of-plane and in-plane thermal conductivity of superlattice thin films, while a 30 μm wide detector is almost insensitive to the component of in-plane thermal conductivity of thin films. Ju *et al.*¹⁸ used a two-wire 3ω method to test the out-of-plane and in-plane thermal conductivity of thin films and composite structures. The film thickness was 1.4 μm and was grown on a substrate with high thermal conductivity. Changing the width of the micro-heating detector and the scale ratio of the sample can reflect the anisotropy of the thermal conductivity of the sample material. Yang *et al.*¹⁹ used the same method to measure the thermal conductivity (150–300 K) of Si/Ge superlattices. The measurement apparatus and results are shown in Fig. 6 and Table II.

06 December 2025 08:34:26

2. Fluid and powder materials

The thermal performance characterization of liquids has gradually been applied with the 3ω method.^{20–22} The measurement of fluid thermal conductivity requires addressing two key issues, one

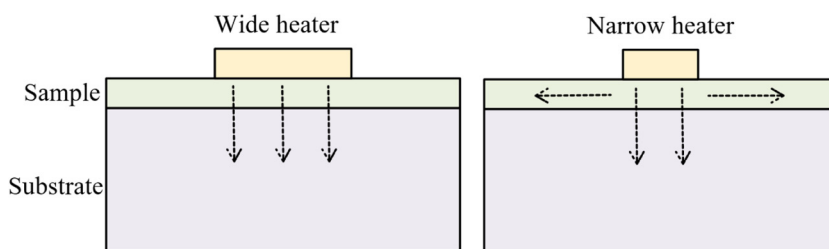
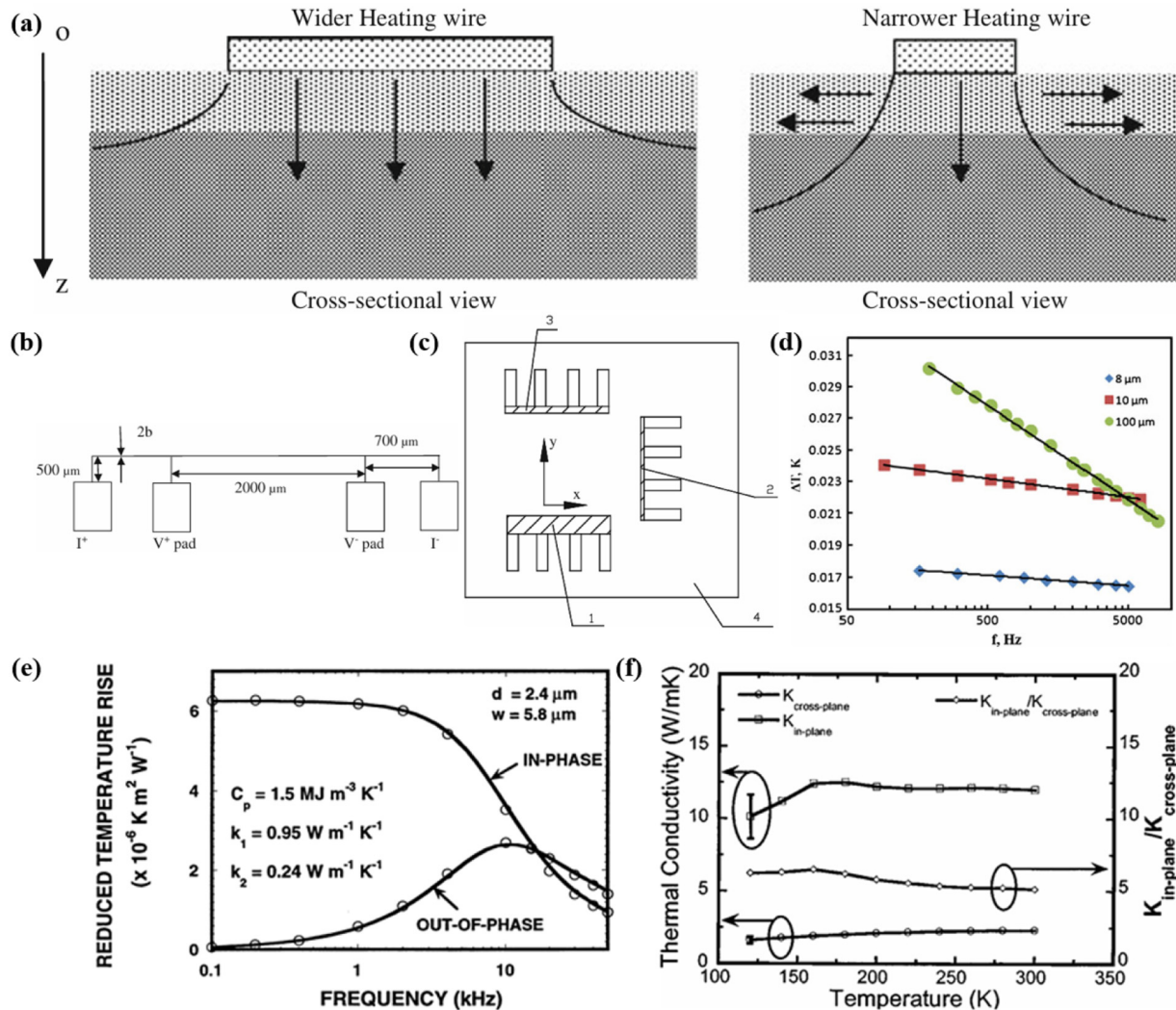


FIG. 4. Internal heat transfer characteristics of the sample.



06 December 2025 08:34:26

FIG. 6. (a) Characteristics of heat conduction in the specimens. (b) Schematic of the four-pad configuration. (c) Arrangement diagram for three microheaters on the surface of the sample. (d) Temperature oscillation amplitudes vs frequency for microheaters.¹⁷ Reproduced from Su *et al.*, Int. J. Thermophys. 34(12), 2334–2342 (2013). Copyright (2013) Springer Nature. (e) Predicted and measured frequency dependence of the temperature rise in a $5.8\ \mu\text{m}$ wide metal line deposited on a $2.4\ \mu\text{m}$ thick polyimide film.¹⁸ Copyright (1999) Elsevier Ltd. (f) In-plane and cross-plane thermal conductivities of the Si/Ge SL as a function of temperature.¹⁹ Reproduced from Yang *et al.*, Appl. Phys. Lett. 81(19), 3588–3590 (2002). Copyright (2002) AIP Publishing LLC.

TABLE II. Solid and anisotropic materials.

Material	Thermal conductivity (W/m K) ^{16–19}
SiC crystal	431.12 (x), 475.47 (y), 389.76 (z)
Si/Ge superlattice	4.7 (in-plane), 5.4 (out-of-plane)
Polyimide films	0.98 (in-plane, $2.4\ \mu\text{m}$ thick), 0.24 (out-of-plane, $2.4\ \mu\text{m}$ thick)
Si/Ge superlattice	12 (in-plane), 2.2 (out-of-plane)

is the insulation of the heating wire and the other is to minimize the impact of natural convection of the liquid. For the problem of insulation, it is necessary to deposit a layer of high-thermal-conductivity insulation film with a thickness of less than $1\ \mu\text{m}$ on the surface of the heating wire. For natural convection problems, increasing the heating frequency with a weak alternating current (a few mA) can reduce the depth of thermal action, thereby weakening the interference caused by convection. The physical model of the line detector is shown in Fig. 7. The measurement principle is

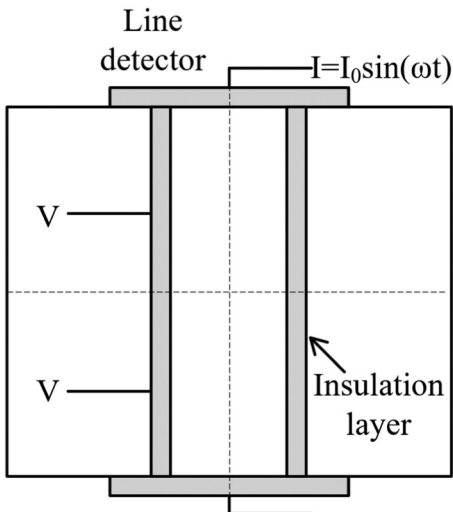


FIG. 7. Physical model of the line detector.

consistent with the bulk material, except for the additional thickness of the insulation layer deposited on the surface of the heating wire. After neglecting the temperature fluctuations of the heating wire and the influence of fluid flow, the formula for calculating the thermal conductivity of liquid can be shown as Eq. (3), where A is the slope of the relationship between temperature fluctuations and phase angle. The selection of the diameter of the heating wire generally satisfies that the product of the reciprocal of the depth of thermal action of the heating wire and the radius of the heating wire is less than 0.3. The length of the heating wire should have a length to diameter ratio greater than 1500,

$$\lambda = -\frac{U_{1\omega}^2}{4\pi lAR_0}. \quad (3)$$

The 3ω method can be used to test the thermal conductivity of liquids by increasing the testing frequency to reduce the impact of convection on the test results. Chen *et al.*²⁰ used immersed Pt wires to test the thermal conductivity and heat capacity of Fc77 liquid, and then tested the thermal conductivity of the solid in the lower part of the liquid. Birge and Nagel²² measured the specific heat of organic liquids as a function of heating frequency in the range of 0.01–3000 Hz using a metal-heating film deposited at the bottom of the container. Wang *et al.*²³ measured the thermal conductivity of nanofluids using a $17\text{ }\mu\text{m}$ diameter platinum wire, 8 mm in length. They found that natural convection effects may be reduced by increasing the frequency of the oscillating current. For the testing of gas thermal conductivity, attention should be paid to the issue of convective interference. Yusibani *et al.*²⁴ used the 3ω method to test the thermal conductivity of gases as shown in Fig. 8. It is found that heat losses from the wire ends have a significant effect on the 3ω components at low frequencies and tend to be less

important at high frequencies. The simplified conventional one-dimensional (1D) model generally presents a larger error which prevents the on-the-spot application of the 3ω method. Research on the measurement of thermal properties of micro/nano-powders using this method is rarely reported. To solve this, Zheng *et al.*²⁵ proposed a simple and practical 3ω slope comparative method by analyzing the relationship among the heat penetration depth, measurement frequency, and detector characteristic parameters. The thermal conductivity of the sample can be accurately obtained by measuring, R_T , $U_{1\omega}$, and k'' (the inverse of the slope for the third harmonic voltage vs logarithm frequency) of the standards (*b*) and the sample (*s*) at different frequencies within the selected frequency band of the same detector. No further calibration of the length, diameter, and electrical resistance of the detector is required based on Eqs. (4) and (5). This method not only eliminates the errors due to calibration but also simplifies the measurement process. Based on the analysis, the effective thermal conductivity of nano-SiO₂ powder is accurately determined. The measurement apparatus and results are shown in Fig. 8 and Table III.

For fluids and powders, thermal convection and contact thermal resistance become significant sources of error that cannot be overlooked during testing. For fluids, an effective approach involves employing narrower metal wires and lower heating currents to minimize temperature rise. The assembly should be positioned in a draught-free, temperature-controlled environment. Placing powder samples within a vacuum chamber for measurement is one of the most effective methods for eliminating the effects of gas convection and conduction. Filling the container with powdered material under constant pressure, or securing the detector before filling with powder, ensures the reproducibility and comparability of data,

$$\lambda_s/\lambda_b = \left(-\frac{\beta U_{1\omega}^2}{8\pi lR_T} \frac{d \ln \omega}{d U_{3\omega}} \right)_s / \left(-\frac{\beta U_{1\omega}^2}{8\pi lR_T} \frac{d \ln \omega}{d U_{3\omega}} \right)_b, \quad (4)$$

$$\lambda_s = \lambda_b \times \left(\frac{U_{1\omega}^2}{R_T} k'' \right)_s / \left(\frac{U_{1\omega}^2}{R_T} k'' \right)_b. \quad (5)$$

3. Thin-film materials

The testing of the thermal conductivity of thin-film materials is similar to that of solid materials, which requires the preparation of a layer of metal detectors on the surface of the tested sample through photolithography or vapor deposition processes. For conductive samples, a 10-nm-thick thin film needs to be deposited on the surface as an insulating layer, and then the detector needs to be prepared on the insulating layer. This requires a smooth and continuous surface of the material, which is not suitable for nanoporous thin-film materials. As early as 1994, Cahill *et al.*²⁶ provided an analytical formula for measuring the thermal conductivity of thin films using the differential method and experimentally measured the thermal conductivity of Si thin films. Afterward, Olson *et al.*²⁷ analyzed the theoretical models of thermal conductivity, thermal diffusivity, and interfacial thermal resistance of multilayer films, and tested the thermal conductivity and thermal diffusivity

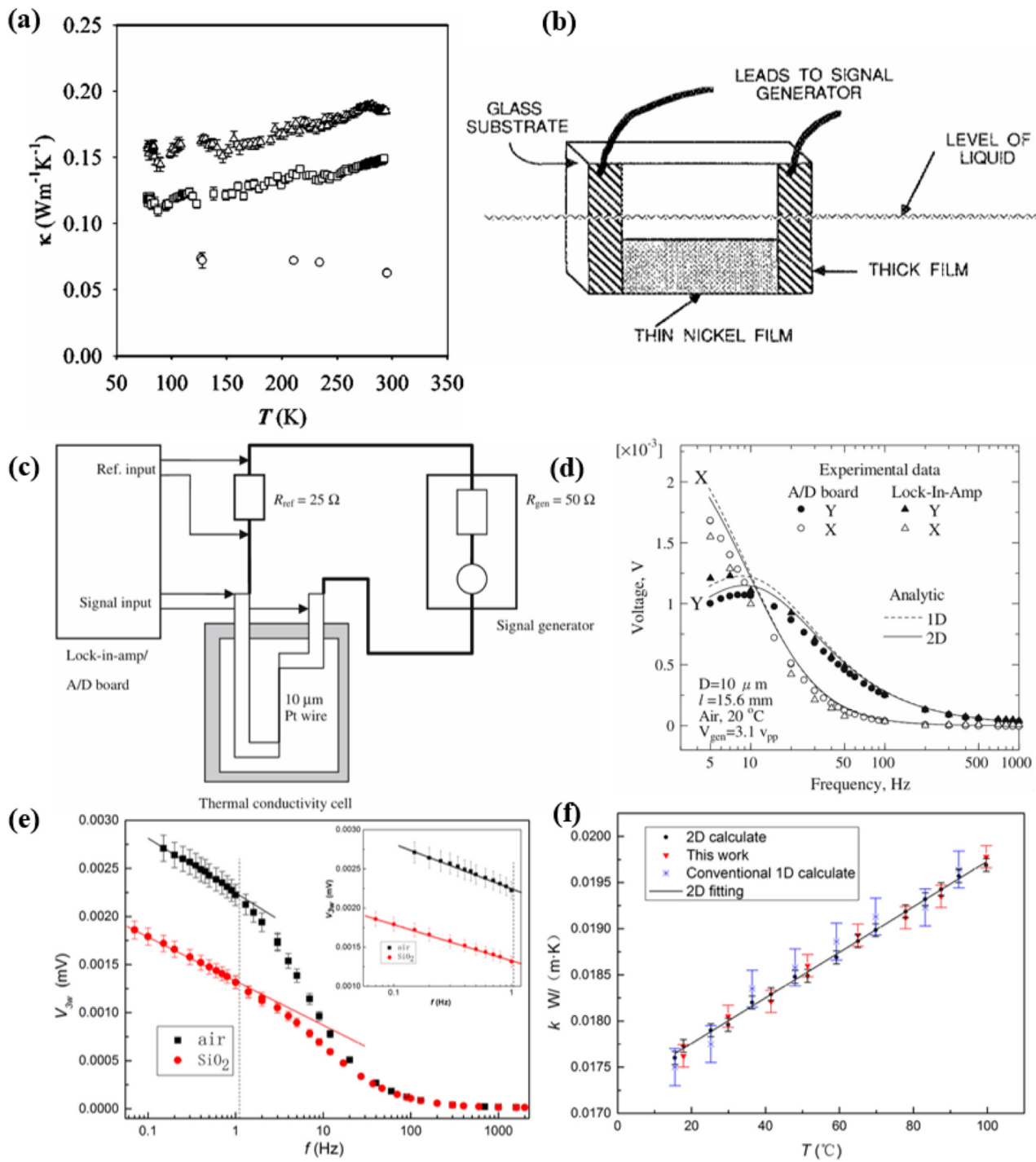


FIG. 8. (a) Thermal conductivity vs temperature at different pressures for the pressure medium FC77.²⁰ Copyright (2004) AIP Publishing LLC. (b) Schematic diagram of the sample heater/thermometer.²² Reproduced from Birge and Nagel, Rev. Sci. Instrum. 58(8), 1464–1470 (1987). Copyright (1987) AIP Publishing LLC. (c) Experimental setup and (d) experimental data compared with the analytical solution.²⁴ Reproduced from Yusibani et al., Int. J. Thermophys. 30(3), 833–850 (2009). Copyright (2009) Springer Nature. (e) Curve for the third harmonic vs logarithm frequency for the air and SiO_2 powder at room temperature and (f) effect of the temperature on the effective thermal conductivity of SiO_2 powder.²⁵ Reproduced from Zheng et al., Mod. Phys. Lett. B 30(25), 1650322 (2016). Copyright (2016) World Scientific Publishing Co. Pte Ltd.

TABLE III. Fluid and powder materials.

Material	Thermal conductivity (W/m K) ^{20,23,25}
FC77 liquid	0.06
TiO ₂ nanofluids	11.9
SiO ₂ nanofluids	1.38
Distilled water	0.625
Ethanol	0.169
Ethylene glycol	0.252
Air	0.026
SiO ₂ powder	0.018

coefficients of multilayer films. Tong and Majumdar²⁸ provided an accurate analytical formula for temperature rise considering the interfacial thermal resistance of thin films and the thermal diffusion effect inside the films. These models and results are shown in Fig. 9 and Table IV. Yao *et al.*²⁹ proposed a software and hardware integration scheme for the 3ω method and tested the thermal conductivity of thin films. The temperature rise signal measured from

TABLE IV. Thermal properties of a borosilicate glass substrate and a 30 μm consolidated zeolite surface film at 300 K and a bulk silicon substrate and a 1.47 mm SiO₂ thermal oxide at 300 K.²⁷

Material	Thermal conductivity (W/m K)
Glass substrate	1.12
Zeolite film	1.07
Silicon substrate	146.1
SiO ₂ film	1.15

thin-film materials is highly dependent on the thermal conductivity of the substrate. The substrate's thermal conductivity value should be inaccurate, and this error will be directly and significantly amplified transferred to the thin-film thermal conductivity. Uncertainties in film thickness and uniformity, the contact between the film and substrate, and the contact between the metal heater and the film all affect the precise measurement of thermal conductivity. Fabricating metal heaters of varying widths on the same substrate and conducting tests across different frequency bands enables the effective

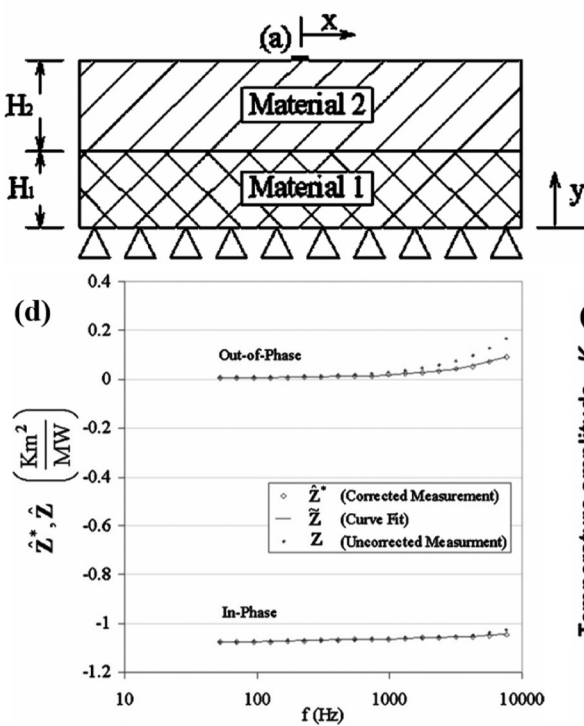


FIG. 9. (a) A two-layer structure with a surfaced patterned 3ω line element. (b) The element is shown in cross section and in-plane views.²⁷ Reproduced from Olson *et al.*, Rev. Sci. Instrum. **76**(5), 053901 (2005). Copyright (2005) AIP Publishing LLC. (c) A more general multilayer system.²⁸ Tong and Majumdar, Rev. Sci. Instrum. **77**(10), 104902 (2006). Copyright (2006) AIP Publishing LLC. (d) Ratio of measured vs corrected surface impedance for a glass/zeolite structure.²⁷ Reproduced from Olson *et al.*, Rev. Sci. Instrum. **76**(5), 053901 (2005). Copyright (2005) AIP Publishing LLC. (e) Numerical evaluation of the temperature responses of a film-on substrate system for the whole relevant frequency range.²⁸ Reproduced from Tong and Majumdar, Rev. Sci. Instrum. **77**(10), 104902 (2006). Copyright (2006) AIP Publishing LLC.

06 December 2025 08:34:26

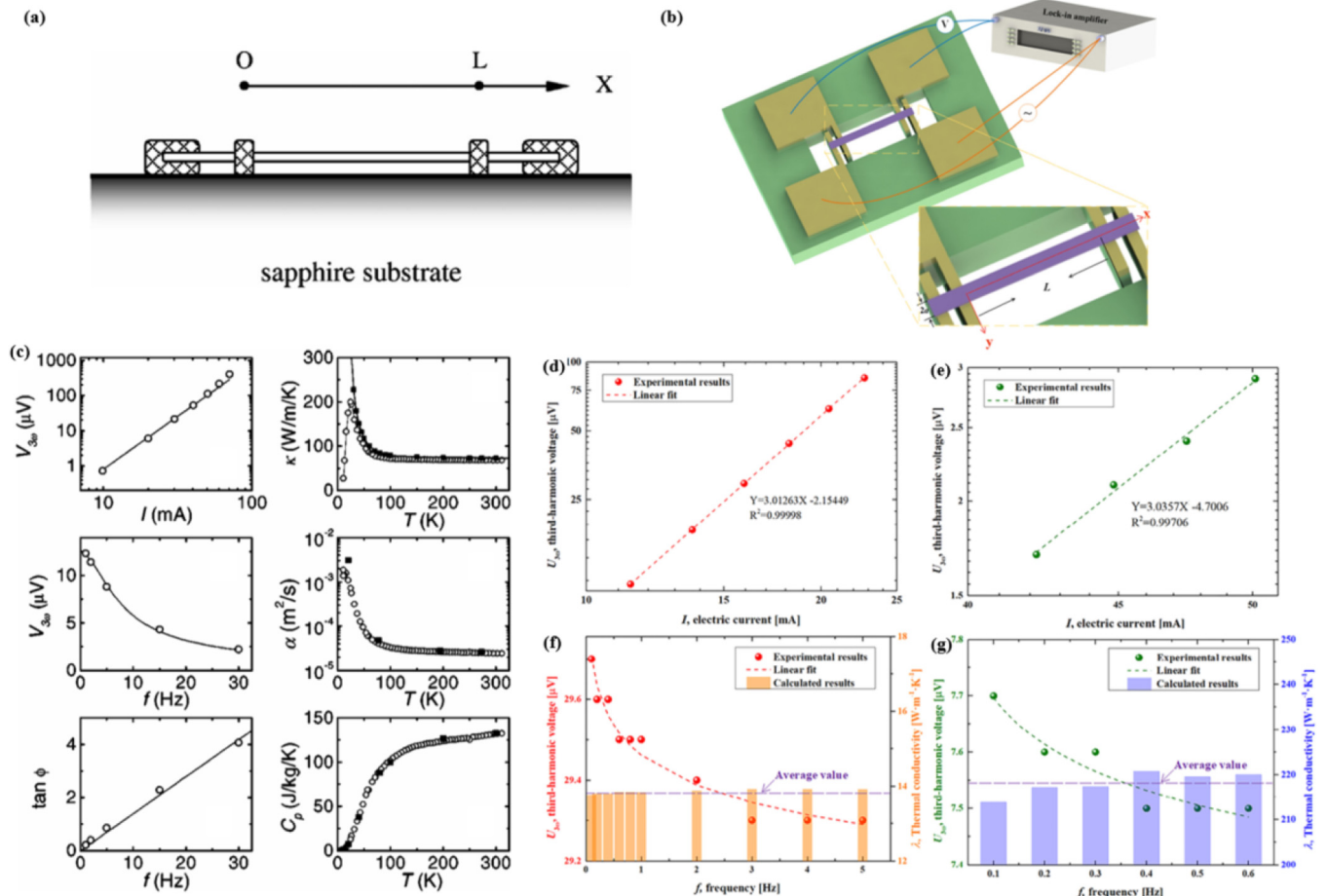


FIG. 10. (a) and (b) Measurement model and principle.^{30,31} (c) Experimental test of the 3ω method on a platinum wire of $20\text{ }\mu\text{m}$ in diameter.³⁰ Reproduced from Lu *et al.*, Rev. Sci. Instrum. **72**(7), 2996–3003 (2001). Copyright (2001) AIP Publishing LLC. (d) and (f) Experimental results of thin sheet materials.³¹ Reproduced from Yang *et al.*, J. Appl. Phys. **137**(17), 175102 (2025). Copyright (2025) AIP Publishing LLC.

determination of thin-film thermal conductivity and interfacial thermal resistance.

4. Fiber and thin sheet materials

The application of an AC signal to a one-dimensional fiber specimen induces temperature oscillations, which is linked to the thermal properties. Based on the 3ω method, Lu *et al.*³⁰ developed a four-point probe measurement technique as shown in Fig. 10. By integrating exact solutions of the one-dimensional heat conduction equation with signal detection via digital lock-in amplification, this approach enables high-precision measurement of thermal conductivity and specific heat capacity in micro/nanoscale one-dimensional materials. The accuracy of this method was verified by platinum wire samples. The measurement requires four high-thermal-conductivity probes and must be conducted within a high-vacuum environment to minimize convective heat loss. As

governed by heat transfer theory, the heat generation and diffusion along the specimen axis are described by the following equation with the associated initial and boundary conditions:

$$\rho C_p \frac{\partial}{\partial t} T(x, t) - \lambda \frac{\partial^2}{\partial x^2} T(x, t) = \frac{I_0^2 \sin^2 \omega t}{LS} [R + R'(T(x, t) - T_0)], \quad (6)$$

$$\begin{cases} T(0, t) = T_0, \\ T(L, t) = T_0, \\ T(x, -\infty) = T_0, \end{cases} \quad (7)$$

where ρ , C_p , λ , L , S , and R represent density, specific heat, thermal conductivity, length, cross section, and electrical resistance of samples, respectively. Furthermore, the measurement necessitates strict boundary condition compliance. Primarily, the specimen and

TABLE V. Fiber and thin sheet materials.

Material	Thermal conductivity (W/m K) ³⁰⁻³²
Platinum wire	~66.7
Porous polyimide fibers	0.06–0.15
Stainless-steel sheet	13.85
Aluminum foil sheet	218.14

detectors must maintain at fixed temperatures. Monitoring whether the functional relationships of $U_{3\omega} - I^3$ and $U_{3\omega} - f$ satisfy the boundary conditions. Secondarily, the specimen temperature must be modulated at a constant rate while sweeping the excitation frequency. The maximum permissible frequency is constrained by 4. Verification $\tan \varphi$ is proportional to the frequency.

The 3ω method intrinsically requires the fiber specimen to serve as both the measured sample and detector, necessitating electrical conductivity. For non-conductive fiber materials, it is difficult to measure directly by the 3ω method. This limitation is overcome by applying a metal coating. Qiu *et al.*³² demonstrated precise axial thermal conductivity measurement of single non-conductive porous polyimide (PPI) fibers via platinum deposition and a modified 3ω technique. Building upon Lu's governing equations,³⁰ the composite thermal conductivity λ_{sp} of the platinum-coated fiber is calculated as

$$\lambda_{sp} \approx \frac{4I_{1\omega}^3 LR^2 \alpha_{CR}}{\pi^4 S U_{3\omega} \sqrt{1 + (\tan \varphi)^2}}, \quad (8)$$

$$\lambda_{sp} = \beta \lambda_{Pt} + (1 - \beta) \lambda_{fiber}, \quad (9)$$

where β denotes the cross-sectional area ratio of the platinum coating to the fiber core. Additionally, it is also necessary to verify the function relationship between $U_{3\omega}$, I^3 , f , and $\tan \varphi$ that satisfy the boundary conditions.

When applying the 3ω method to sheet materials, conventional electrode deposition imposes strict surface roughness requirements. Yang *et al.*³¹ overcame this limitation through a

novel two-dimensional thermal conduction model. This approach eliminates surface constraints by reformulating the transient heat conduction differential equation,

$$\lambda \approx \frac{32I_{1\omega}^3 LR^2 \alpha_{CR} a^2}{\pi^6 S U_{3\omega} (L^2 + a^2)} \frac{1}{1 + \cot^2 \theta}, \quad (10)$$

where α_{CR} is the temperature coefficient of resistance, R is the resistance, $I_{1\omega}$ is the 1ω current, L is the length, a is the half-width, $U_{3\omega}$ is the 3ω voltage amplitude, and S is the cross-sectional area. The detector is fabricated using printed circuit board (PCB) technology, featuring selectively copper-plated signal traces with suspended structures to minimize conductive heat loss. The experimental process and boundary condition verification strictly followed Lu *et al.*'s work.³⁰ The experimental results of fiber and thin sheet materials are shown in Table V. Testing errors in fibers and sheet materials primarily stem from contact errors and radiant heat loss. The use of suspended electrodes and established micro/nanofabrication techniques for electrode fabrication can effectively mitigate contact issues. The proportion attributable to radiation-induced components requires specific analysis.

B. Independent detectors of the 3ω method

Conventional 3ω methods have some inherent drawbacks, such as cumbersome and repetitive electrode deposition processes, and the existence of some material surfaces on which electrodes cannot be deposited. In addition, the deposited electrodes are fragile and easily damaged. These drawbacks limit the further application of the 3ω method.

To overcome the difficulties of the previous section, Qiu *et al.*³³ developed a symmetrically modeled free-standing detector for polyimide films. This free-standing detector uses a $25\text{ }\mu\text{m}$ DuPont Kapton HN film as the substrate, and a nickel strip and four metal pads are deposited on the substrate. After soldering the wires to the pads, the nickel tape was encapsulated by hot pressing another piece of film onto the substrate surface, making the free-standing detector reusable, as shown in Fig. 11(a). However, due to

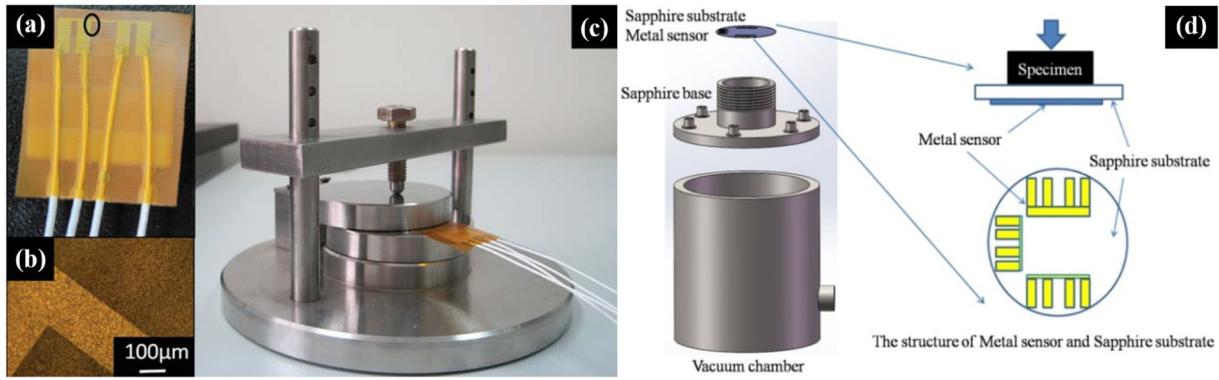


FIG. 11. (a)–(c) HN films free-standing detector.³³ Reproduced from Qiu *et al.*, Rev. Sci. Instrum. **82**(4), 045106 (2011). Copyright (2011) AIP Publishing LLC LLC. (d) Sapphire substrate free-standing detector.³⁴ Reproduced from Zheng *et al.*, Rev. Sci. Instrum. **89**(8), 084904 (2018). Copyright (2018) AIP Publishing LLC.

the softness and low thermal diffusivity of the polyimide film, the metal electrodes are easily damaged during the measurement process, and the time cost of the measurement is too high because of the need to set a very low measurement frequency. On this basis, Zheng *et al.*³⁴ invented a sapphire substrate free-standing detector. The detector is a one-sided model. The detector uses a 100 μm polished sapphire substrate as a base and a nickel metal sensor on the side of the sapphire substrate using photolithography and CVD processes. The sensors were packed in a vacuum chamber to form a stethoscope type standalone detector as shown in Fig. 11(b). Due to the use of high hardness and wear-resistant sapphire as the substrate, it can further prevent the metal electrodes from being destroyed, but there is still the problem that sapphire is fragile. And due to the large thermal diffusivity of sapphire, the frequency setting during the measurement process is relatively high compared to the polyimide substrate, which significantly reduces the time cost.

The temperature rise in the strip when measurements are made by both independent detectors is described using a simplified form of the two-dimensional, two-layer heat transfer equation derived by Borca-Tasciuc *et al.*³⁵ The temperature distribution in the sapphire substrate detector can be described as

$$\Delta T = -\frac{p}{\pi l \lambda_{y,1}} \int_0^\infty \frac{1}{A_1 B_1} \frac{\sin^2(bm)}{(bm)^2} dm, \quad (11)$$

$$A_1 = -\frac{\frac{\lambda_{y,2} B_2}{\lambda_{y,1} B_1} + \tanh(\eta_1)}{1 + \frac{\lambda_{y,2} B_2}{\lambda_{y,1} B_1} \tanh(\eta_1)}, \quad (12)$$

$$B_1 = \left(\lambda_{xy,1} m^2 + \frac{i2\omega}{\alpha_{y,1}} \right)^{1/2}, \quad (13)$$

$$B_2 = \left(m^2 + \frac{i2\omega}{\alpha_{y,1}} \right)^{1/2}, \quad (14)$$

$$\eta_1 = B_1 d_1, \quad (15)$$

$$\lambda_{xy,1} = \frac{\lambda_{x,1}}{\lambda_{y,1}}. \quad (16)$$

In Eqs. (11)–(16), the subscript y corresponds to the direction perpendicular to the interface between the substrate and the specimen (the cross-plane), subscript 1 corresponds to the substrate, subscript 2 corresponds to the specimen, b is the strip half-width, m is the integration factor, λ is the thermal conductivity, p/l is the peak electrical power per unit length, ω is the angular frequency of the alternating current, d is the thickness, λ_{xy} is the ratio of the in-plane to the cross-plane thermal conductivity of the film, and α is the thermal diffusivity.

Based on the above equations, it is possible to experiment with the temperature rise (ΔT_m),

$$\Delta T_m = \frac{2V_{3\omega}}{V_{1\omega}\alpha_{CR}}. \quad (17)$$

In Eq. (17), $V_{1\omega}$ and $V_{3\omega}$ denote the measured 1ω and 3ω voltages, respectively, and α_{CR} denotes the resistance temperature rise coefficient of the sensor.

Since a two-dimensional heat diffusion effect occurs in the substrate, the heat flux needs to be corrected, and the measurement error can be effectively reduced by introducing the effective heat flow ratio S ,^{34,36}

$$S = \frac{p_{y,2}}{p} = \frac{2}{\pi} \int_0^\infty \frac{\sin^2(m)}{m^3} \frac{\tanh(\beta_1 m) \tanh(\beta_2 m)}{\beta_1 \left[\tanh(\beta_2 m) + \sqrt{\lambda_{x,1} \lambda_{y,1}} \tanh(\beta_1 m) \right]} dm, \quad (18)$$

$$\beta_1 = \sqrt{\lambda_{xy,1}} \frac{d_1}{b}, \quad (19)$$

$$\beta_2 = \frac{d_2}{b}. \quad (20)$$

In the formula for the effective heat flow ratio S , d is the thickness, b is the half-width of the sensor, subscript 1 denotes the substrate, subscript 2 denotes the specimen, and x and y denote the transverse and longitudinal directions of the substrate, respectively.

Equation (11) is corrected by introducing an effective heat flow ratio,

$$\Delta T = -\frac{p}{\pi l \lambda_{y,1}} \int_0^\infty \frac{1}{A_1 B_1} \frac{\sin^2(bm)}{(bm)^2} dm \times S. \quad (21)$$

The thermal conductivity of the specimen is calculated as

$$\lambda_s = \frac{V_{1\omega}^3 \alpha_{CR}}{4\pi l R} \times \frac{1}{k} \times S. \quad (22)$$

In the equation, λ_s is the thermal conductivity of the specimen, R is the resistance of the sensor, l is the length of the sensor, and k is the slope of the third harmonic voltage of the metal sensor with respect to the logarithmic coordinate of the frequency.

Compared to the sapphire substrate free-standing detector, the HN film detector is a symmetric model,³⁴ and, therefore, its temperature distribution describes a slightly different model than Eq. (11),

$$\Delta T = -\frac{p}{2\pi l \lambda_{y,1}} \int_0^\infty \frac{1}{A_1 B_1} \frac{\sin^2(bm)}{(bm)^2} dm. \quad (23)$$

1. Solid materials

For both detectors, the thickness of the specimen should be greater than the penetration depth of the heat wave to ensure that the theoretical model is applicable. During the characterization of thermal properties of solid materials, the HN thin-film detector needs to be sandwiched between two identical specimens and clamped using a sample holder. In addition, the contact surfaces between the two specimens and the detector need to be polished to minimize the contact resistance. To ensure that the heat wave

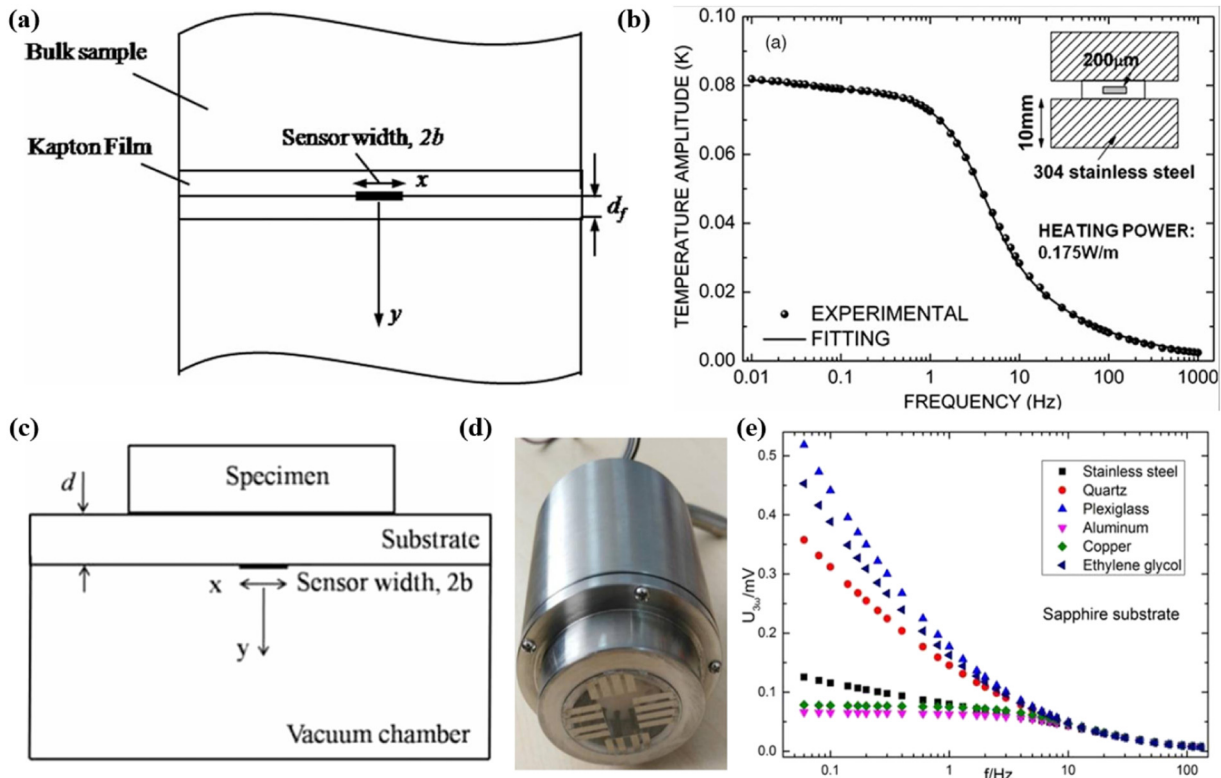


FIG. 12. (a) Schematic for a typical solid characterization configuration with a 3ω free-standing sensor. (b) Temperature amplitudes of the free-standing sensor measuring 304 stainless steels for the whole relevant frequency range.³³ Reproduced from Qiu *et al.*, Rev. Sci. Instrum. **82**(4), 045106 (2011). Copyright (2011) AIP Publishing LLC. (c) Schematic for a measuring structure with a 3ω independent detector. (d) Sapphire substrate independent detector. (e) Third harmonic measurement curve of the sapphire independent detector at different frequencies.³⁴ Reproduced from Zheng *et al.*, Rev. Sci. Instrum. **89**(8), 084904 (2018) Copyright (2018) AIP Publishing LLC.

06 December 2025 08:34:26

penetrates the polyimide film, the frequency setting during the measurement is usually lower than 1 Hz, and in practice is generally less than 0.1 Hz. The scanning time constant during the measurement should be set sufficiently large (at least five times the period of the heated alternating current) to ensure that weak signals at low frequencies can be prepared to be detected. Compared to the HN film detector, the sapphire detector is encapsulated in the steel base, so that it can be used to reduce the contact thermal resistance between the detector and the specimen by its own weight during the measurement of solid materials, without the need for external assistance. However, it is still necessary to polish the sample surface during the measurement. In practice, due to the greater thermal diffusivity of the sapphire substrate, the measurement frequency is generally set to 1–10 Hz. The test results from the two detectors are shown in Fig. 12.

2. Fluid and powder materials

For thermal conductivity measurements of liquids or powders, the free-standing detector is placed in the specimen, where it is necessary to ensure that the thickness and width of the liquid or powder specimen are much greater than the depth and width of the thermal

wave penetration, respectively. For the HN film detector, due to the limitations of its substrate material, the detector is unable to realize the measurement of temperatures above 150 °C and unable to complete the measurement of some corrosive liquids. When measuring powder materials, the particle size of the specimen should not be too large and the hardness should not be too high for either detector. Otherwise, the applied stress may be too high, causing the HN film detector to deform and fail or the sapphire detector to rupture. The test results for fluids and powders are shown in Fig. 13.

3. Thin-film materials

The theoretical model for measurements with HN film detectors is different from that for bulk materials for smaller film specimens (tens of micrometers), i.e., thicknesses less than the penetration depth of the heat wave. To measure membrane materials with thinner thicknesses, a symmetric five-layer system (substrate-specimen-sensor-specimen-substrate) and a three-layer system (substrate-sensor-substrate) were developed by Qiu *et al.*³⁷ in 2015. In this system, the specimen is symmetrically sandwiched between the independent sensor and the substrate. The substrate is used to provide an isothermal boundary condition and to flatten

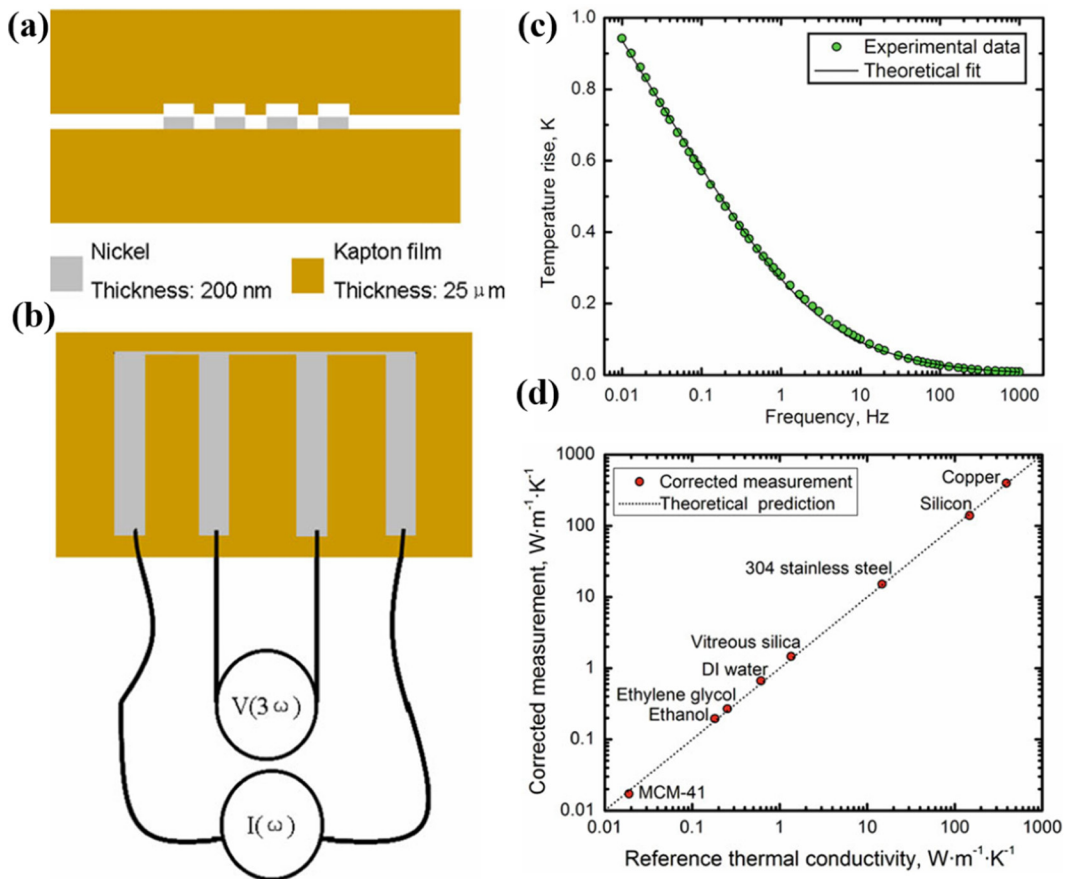


FIG. 13. (a) Schematic diagram of the free-standing sensor based on the 3ω technique. The element is shown in (a) cross section and (b) in-plane views. (c) Experimental temperature rise and the fitting based on the two-dimensional heat conduction model for ethylene glycol measured by the free-standing sensor. (d) Experimental results of the thermal conductivity for fluid and powder materials.³⁰ Reproduced from Qiu *et al.*, Int. J. Thermophys. 34(12), 2261–2275 (2013). Copyright (2013) Springer Nature.

06 December 2025 08:34:26

the membrane to achieve good contact with the sensor. Substrates are typically chosen from high-thermal-conductivity materials such as 304 stainless steels. By comparing the difference in temperature response between the five-layer system and the three-layer system, the thermophysical properties of the specimen can be obtained, as shown in Fig. 14.

The solution for the complex temperature rise (ΔT) of the independent sensors of the symmetric five-layer system can likewise be described as a simplified form of the generalized two-dimensional multilayer heat transfer equation derived by Borca-Tasciuc *et al.*,²⁴ as shown in Eq. (23). The formulas for the other parameters are changed as follows:

$$A_{i-1} = - \frac{A_i \frac{\lambda_{y,i} B_i}{\lambda_{y,i-1} B_{i-1}} + \tanh(\eta_{i-1})}{1 - A_i \frac{\lambda_{y,i} B_i}{\lambda_{y,i-1} B_{i-1}} \tanh(\eta_{i-1})}, \quad i = 2, 3, \quad (24)$$

$$B_i = \left(\lambda_{xy,i} m^2 + \frac{i 2\omega}{\alpha_{y,i}} \right)^{1/2}, \quad i = 1, 2, 3, \quad (25)$$

$$\eta_i = B_i d_i, \quad (26)$$

$$\lambda_{xy,i} = \frac{\lambda_{x,i}}{\lambda_{y,i}}. \quad (27)$$

In the above Eqs. (24)–(27), subscripts 1, 2, and 3 correspond to the flexible insulating layer of the free-standing sensor, the specimen, and the substrate, respectively. Since the substrate is semi-infinite $A_3 = -1$.

For a three-layer system, the temperature rise (ΔT^*) can be expressed as

$$\Delta T^* = - \frac{p}{2\pi l \lambda_{y,1}} \int_0^\infty \frac{1}{A_1^* B_1} \frac{\sin^2(bm)}{(bm)^2} dm, \quad (28)$$

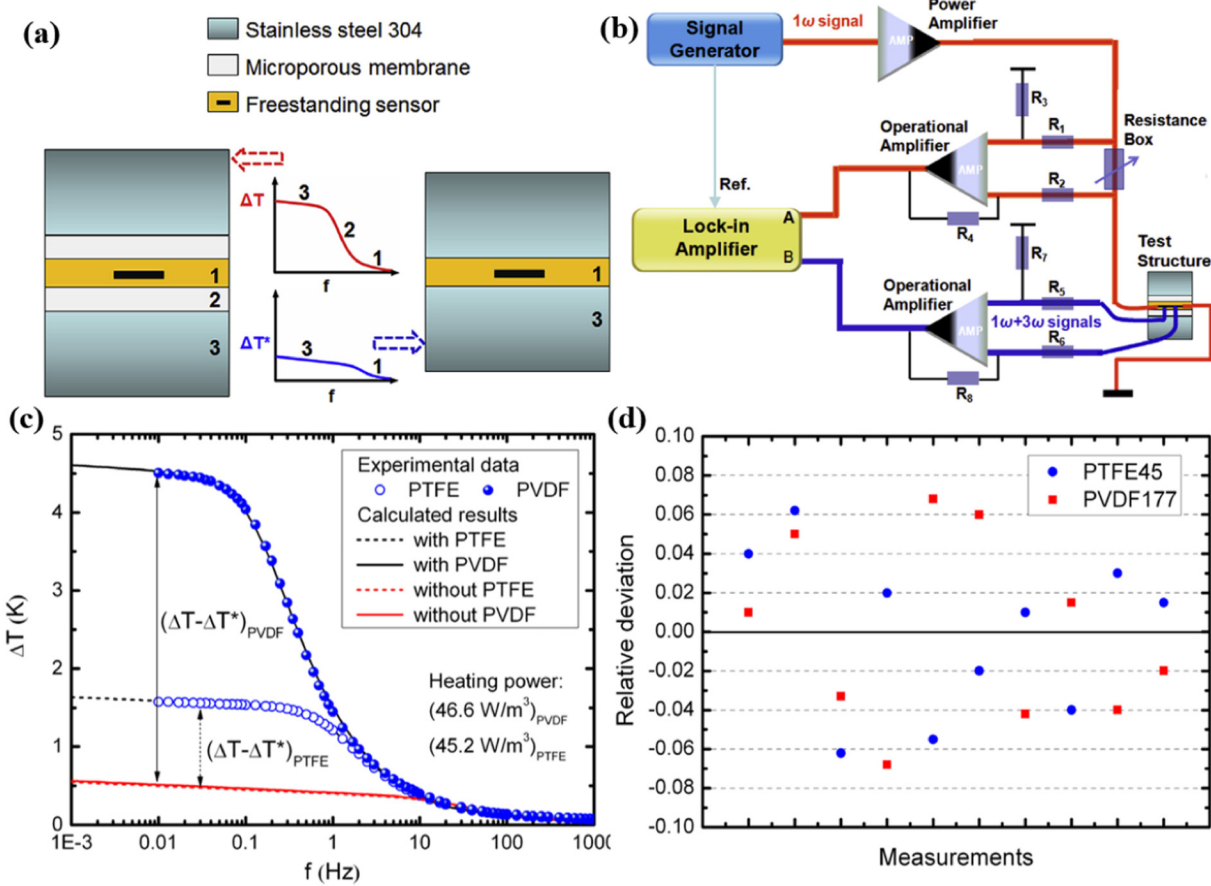


FIG. 14. (a) The symmetric five-layer system (substrate–specimen–sensor–specimen–substrate) and the three-layer system (substrate–sensor–substrate). (b) Schematic representation of the free-standing sensor-based 3ω technique for measurement of microporous membranes. (c) Temperature amplitudes of the free-standing sensor measuring PTFE45 and PVDF177 membranes. (d) Deviation of the experimental data for PTFE45 and PVDF177 membranes.³⁷ Reproduced from Qiu *et al.*, Int. J. Therm. Sci. **89**(3), 185–192 (2015). Copyright (2015) Elsevier Ltd.

06 December 2025 08:34:26

$$A_1^* = -\frac{A_3^* \frac{\lambda_{y,3} B_3}{\lambda_{y,1} B_1} + \tanh(\eta_1)}{1 - A_3^* \frac{\lambda_{y,3} B_3}{\lambda_{y,1} B_1} \tanh(\eta_1)}. \quad (29)$$

Combining the thermally conductive substrate assumption and the insulating film assumption, the temperature difference between the two systems when the AC frequency is low can be expressed as

$$\Delta T - \Delta T^* = -\frac{p}{2\pi l \lambda_{y,1}} \int_0^\infty \left(\frac{1}{A_1} - \frac{1}{A_1^*} \right) \frac{1}{B_1} \frac{\sin^2(bm)}{(bm)^2} dm = \frac{pd_2}{4bl\lambda_{y,2}}. \quad (30)$$

The above equation shows that when the frequency is very low, the presence of the film only introduces a frequency-independent temperature rise to the thermal response ΔT^* of the substrate.

In the experimental measurements, the temperature rise of the five-layer system can be calculated by Eq. (17), and the temperature rise of the three-layer system can be calculated by Eq. (28). At low frequencies (generally below 0.06 Hz), the thermal conductivity of the film can be calculated by Eq. (30). When measuring the thermal conductivity of thin films (tens of micrometers) using this method, if the depth of thermal penetration is not large enough compared to the thickness of the film, the assumption that the presence of the film only introduces a frequency-independent temperature rise is invalid, i.e., Eq. (30) does not hold. It is necessary to ensure that the heat wave can penetrate the film during the measurement, and there is an upper thickness limit for the technique to measure the thermal conductivity of the film.

4. Anisotropic materials

For thermal conductivity measurements of anisotropic materials, it is necessary to encapsulate sensors with different widths in the HN film free-standing detectors, as shown in Fig. 15.

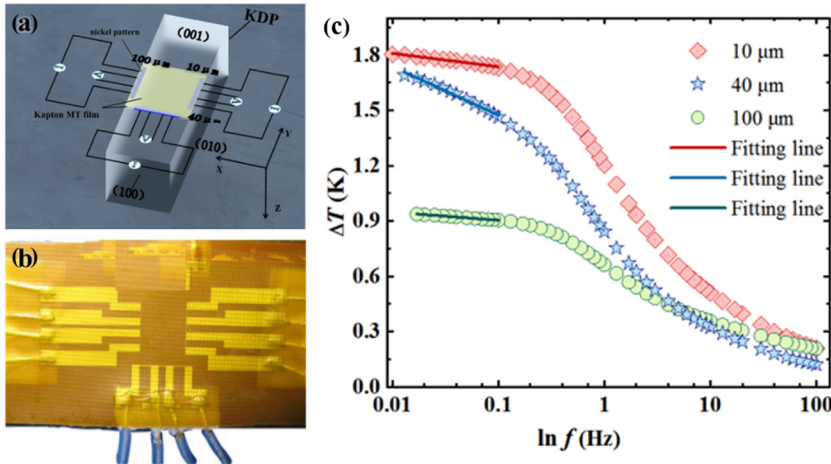


FIG. 15. (a) and (b) HN film free-standing detector for measuring thermal conductivity of anisotropic materials and schematic diagram for measuring KDP crystals by Qiu *et al.* (c) The fitted results of temperature rise as a function of frequency.³⁸ Reproduced from Qiu *et al.*, Sensors **21**(23), 7968 (2021). Copyright (2021) MDPI.

The temperature change of the individual sensors in the detector during the measurement can be calculated using Eq. (17). Based on Borca-Tasciuc's³⁵ analytical solution for the average temperature rise of the sensor, the measurement principle can be expressed by the following equation:

$$\Delta T = \frac{p_1}{\pi \sqrt{\lambda_z \lambda_y}} \left[0.5 \ln \frac{\lambda_y}{Cb^2} - 0.5 \ln (\omega) + \gamma - \frac{i\pi}{4} \right], \quad (31)$$

$$\Delta T = \frac{p_1}{\pi \sqrt{\lambda_x \lambda_z}} \left[0.5 \ln \frac{\lambda_x}{Cb^2} - 0.5 \ln (\omega) + \gamma - \frac{i\pi}{4} \right]. \quad (32)$$

In the above equation, p_1 is the heating power per unit length of the sensor; i is the imaginary component; ω is the heating frequency; C is the volume of the heat capacity; b is the half-width of the patterns; γ is the constant; and λ_x , λ_y , and λ_z are the thermal conductivities in the x , y , and z directions, respectively. In the measurement, the thermal conductivity in the z -direction is first measured and then solved for in the x - and y -directions by bringing in Eqs. (31) and (32), respectively.

During the measurement, to ensure that the simplified formula is valid, the heater needs to be a linear heat source, and, therefore, it needs to be ensured that the depth of penetration of the heat wave meets the requirement of at least five times the half-width of the heater. The width of the heater should be customized for different materials.

5. Rough surfaces

In addition to the HN film free-standing detector and the sapphire free-standing detector, a PMMA free-standing detector was prepared by Kong *et al.*³⁹ in 2018. The measurement of thermal conductivity of rough surface materials bridged by vertically aligned CNT arrays (primary CNTs) and randomly oriented secondary CNTs was realized by this detector. The structure of the detector is shown in Fig. 16.

The PMMA free-standing sensor consists of a PMMA substrate, a metal heater, and an insulating layer of silicon nitride (Si_3N_4). The PMMA enables effective thermal insulation. The Si_3N_4 layer acts as an insulator. Measurements using this method require the numerical extraction of the thermal conductivity of the material and the contact resistance between the sensor and the sample surface with the aid of a finite element model. This method requires numerical extraction of thermal conductivity as well as contact resistance with the help of a finite element model.

The controlled heat equations for the heater, free-standing sensor (PMMA), specimen, and substrate are

$$\frac{\partial}{\partial x} \left(\lambda_h \frac{\partial T_h}{\partial x} \right) + \frac{\partial}{\partial y} \left(\lambda_h \frac{\partial T_h}{\partial y} \right) + p = \rho C \frac{\partial T_h}{\partial t}, \quad (33)$$

$$\frac{\partial}{\partial x} \left(\lambda_{\text{PMMA}} \frac{\partial T_{\text{PMMA}}}{\partial x} \right) + \frac{\partial}{\partial y} \left(\lambda_{\text{PMMA}} \frac{\partial T_{\text{PMMA}}}{\partial y} \right) = \rho C \frac{\partial T_{\text{PMMA}}}{\partial t}, \quad (34)$$

$$\frac{\partial}{\partial x} \left(\lambda_s \frac{\partial T_s}{\partial x} \right) + \frac{\partial}{\partial y} \left(\lambda_s \frac{\partial T_s}{\partial y} \right) + p = \rho C \frac{\partial T_s}{\partial t}, \quad (35)$$

$$\frac{\partial}{\partial x} \left(\lambda_{\text{sub}} \frac{\partial T_{\text{sub}}}{\partial x} \right) + \frac{\partial}{\partial y} \left(\lambda_{\text{sub}} \frac{\partial T_{\text{sub}}}{\partial y} \right) + p = \rho C \frac{\partial T_{\text{sub}}}{\partial t}. \quad (36)$$

In the above equation, p is the heat generation rate of the sensor, λ is the thermal conductivity, ρ is the density, and C is the heat capacity.

In the solution process, the oscillation temperature of the heater ΔT was obtained by calculating the average oscillation temperature over the width of the heater [Eq. (17)]. The thermal conductivity (λ_s) and contact resistance (R_c) were varied iteratively until the simulation results matched the experimental data using the least mean square fit of the Comsol optimization solver.

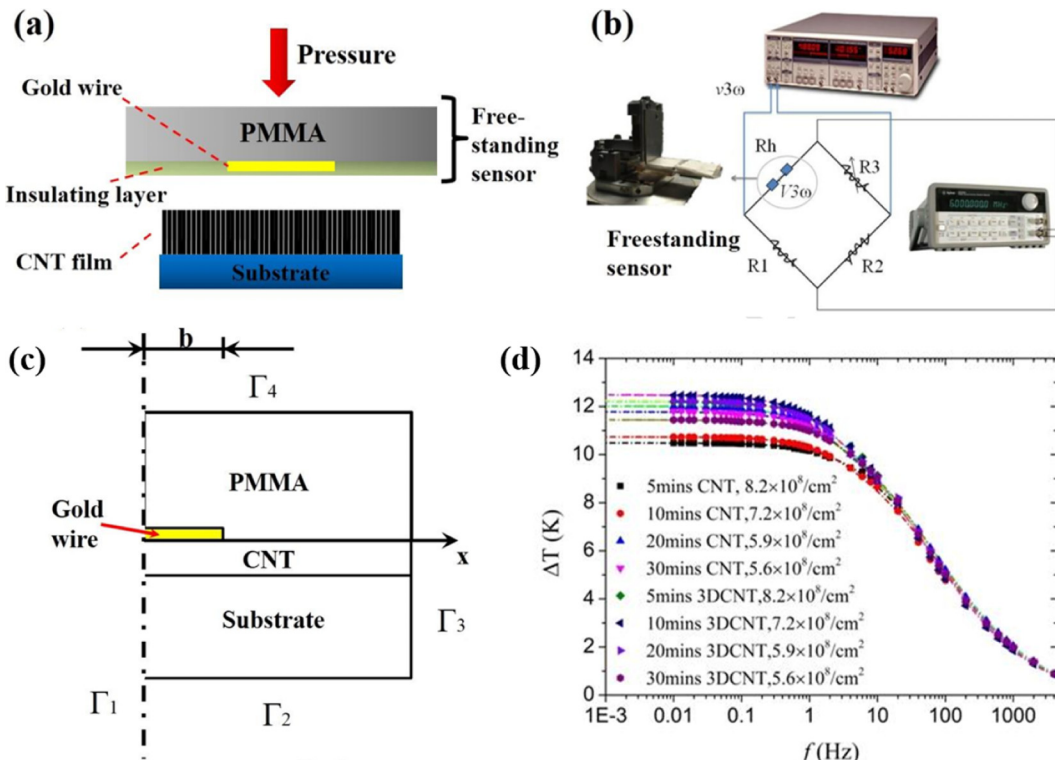


FIG. 16. (a) The structure of the PMMA free-standing detector. (b) The electrical circuit of 3ω technique. (c) A schematic view of the 2D thermal model with a symmetry plane Γ_1 . (d) The temperature rise of the free-standing sensor as a function of the frequency for primary CNT arrays and 3D CNT network.³⁹ Reproduced from Kong *et al.*, Surf. Coat. Technol. **345**, 105–112 (2018). Copyright (2018) Elsevier Ltd.

06 December 2025 08:34:26

When taking measurements using this method, it is important to ensure that the length of the wire is much greater than the depth of thermal penetration. This ensures a uniform temperature along the wire's length and validates the use of a two-dimensional (2D) thermal diffusion model in a plane perpendicular to the wire's axis. Figure 17 and Table VI demonstrate the measurement results of different independent detectors for different materials and the comparison with literature values.

C. Thermoelectric integrated measurement of the 3ω method

For micro/nano materials such as thin films and fibers, their properties are affected by a variety of factors such as geometry, size, and surface topography. Current preparation and transfer techniques cannot achieve a high degree of uniformity among multiple samples. This may result in errors when the properties of different samples are characterized separately. Therefore, integrated characterization of the thermoelectric properties of materials is necessary.

1. Thin film analyzers

A Thin Film Analyzer (TFA) instrument can be used to characterize thin-film samples, enabling integrated measurement of

multiple thermoelectric parameters. It is a highly integrated and easy-to-use commercial measurement instrument. The basic configuration of the TFA consists of two parts: a measurement chip and a measurement chamber. Samples can be conveniently deposited onto the measurement chip. This chip allows for sample preparation via physical vapor deposition (PVD, e.g., thermal evaporation, sputtering, molecular beam epitaxy), chemical vapor deposition (CVD, e.g., atomic layer deposition), spin coating, drop casting, or inkjet printing. The measurement chamber provides the required environmental conditions, typically operating under high vacuum. During measurements, utilizing liquid nitrogen and a powerful heater, the sample temperature can be controlled between -160 and 280 °C. This enables integrated measurement of thermoelectric parameters over a wide temperature range.

The TFA instrument utilizes a pre-patterned chip onto which thin-film samples are directly deposited for measurement. The same chip fulfills all parameter testing requirements, as shown in Fig. 18(a). The measurement chip integrates the 3ω method for thermal conductivity measurement with the four-probe van der Pauw method for determining electrical transport properties, while the Seebeck coefficient is measured via resistance thermometers adjacent to the van der Pauw electrodes. Consequently, this system enables the simultaneous measurement of multiple thermoelectric

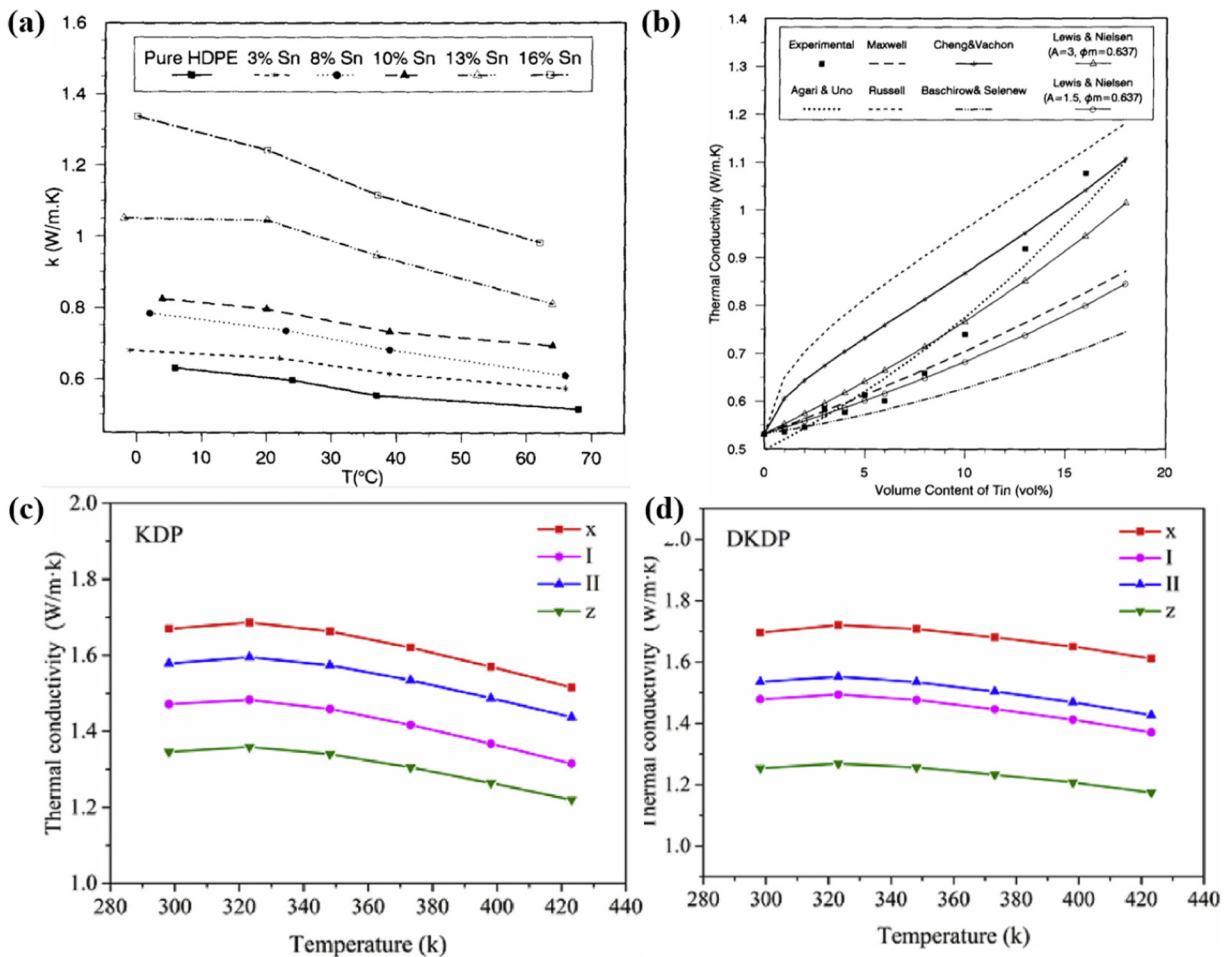


FIG. 17. (a) and (b) Measured thermal conductivity and comparison of the experimental and predicted thermal conductivity values of HDPE filled with tin particles.⁴⁰ Reproduced from Tavman, Int. Commun. Heat Mass Transfer **25**(5), 723–732 (1998). Copyright (1998) Elsevier Ltd. (c) and (d) Thermal conductivity vs temperature curves of KDP and 70%-DKDP crystals.⁴¹ Reproduced from Wang *et al.*, J. Alloys Compd. **790**, 212–220 (2019). Copyright (2019) Elsevier Ltd.

06 December 2025 08:34:26

parameters on a thin-film sample, primarily including the thermal conductivity (λ), electrical resistivity (σ), and Seebeck coefficient (S). Moreover, all measurements are conducted along the identical (in-plane) direction, thereby ensuring high comparability. The thermal conductivity (λ) is determined using the 3ω method, wherein a metal strip serves simultaneously as both a heater and a sensor. Within the same experimental setup, either steady-state (DC) testing or transient testing (3ω) can be employed. However, the 3ω testing technique offers greater precision than the DC method. Applying an alternating current with an angular frequency of 1ω to the resistor results in a voltage signal at the 3ω frequency, from which information about temperature oscillations can be derived. The experimental setup for the 3ω method is shown in Fig. 18(b). An insulating thin film is present between the sample and the metal strip to prevent electrical signal interference. The electrical resistivity of the thin-film sample is measured using the

van der Pauw method. This method can be used with samples of virtually any shape, provided they are uniformly thick and structurally intact with no holes. Furthermore, the geometric shape of the thin-film sample can be precisely defined using a metal shadow mask. The van der Pauw method requires making contacts at the periphery of the sample's four corners, and these contact points must be small relative to the sample size, as shown in Fig. 18(c). The Seebeck effect is a thermoelectric phenomenon manifested as an electrical voltage generated by a temperature difference. The ratio of these two quantities defines the Seebeck coefficient, which is an intrinsic property of the material itself. The thin-film sample contacts a heater strip. When the sample is heated, a temperature difference is established across the sample. This temperature difference is measured using a serpentine resistance thermometer, as shown in Fig. 18(d). Simultaneously, the voltage difference between two points is measured via lead electrodes, enabling the calculation

TABLE VI. Experimental measurement results of various specimens.

Specimens	λ (W/m K) ^{33,34,36–39}	λ_{ref} (W/m K) ^{40–44}
Copper	374 (HN); 378 (sapphire)	390
Silicon	140 (HN)	148
304 Stainless steel	14.1 (HN); 15.4 (sapphire)	14.8
Vitreous silica	1.47 (HN); 1.41 (sapphire)	1.35
DI water	0.642 (HN)	0.610
Ethylene glycol	0.237 (HN); 0.265 (sapphire)	0.252
Ethanol	0.192 (HN)	0.182
MCM-41	0.0185 (HN)	0.0201
Plexiglass	0.221 (HN); 0.196 (sapphire)	0.21
Aluminum	226 (HN); 229(sapphire)	237
PTFE45	0.071 ± 0.006 (HN five-layer)	0.068
PVDF177	0.077 ± 0.006 (HN five-layer)	0.070
KDP-x	1.63 ± 0.06 (HN)	1.67
KDP-y	1.38 ± 0.07 (HN)	1.47 (49°); 1.58 (31°)
KDP-z	1.32 ± 0.09 (HN)	1.35

of the Seebeck coefficient. Thus, the acquisition of parameters such as thermal conductivity, Seebeck coefficient, and electrical conductivity on the thin-film sample is achieved, allowing for the direct calculation of the thermoelectric figure of merit (ZT). In addition, the pre-patterned chip also facilitates the measurement of parameters including the Hall coefficient, specific heat, Hall mobility, and charge carrier density.

The Thin Film Analyzer significantly enhances the testing efficiency for thermoelectric properties of thin-film materials through its pre-structured chip design and multi-parameter integration technology. It supports a wide temperature range from -160 to 280°C , being particularly suitable for miniature samples (thickness ≥ 100 nm). However, thin-film samples are prepared on both

sides of the pre-patterned chip via methods such as spin coating, deposition, or sputtering. This separation necessitates distinct measurements for thermal conductivity vs parameters like electrical conductivity and the Seebeck coefficient, ultimately leading to significant ZT measurement errors. Simultaneously, substantial structural and dimensional variations between individual samples may result in erroneous ZT calculations. Furthermore, the instrument is exclusively applicable to thin-film samples and cannot measure materials such as powders, fluids, or fibers. Moreover, its suspended thin film is extremely fragile, compromising measurement results. Therefore, it is necessary to develop *in situ* comprehensive measurement of thermoelectric performance.

2. *In situ* measurement of thermoelectric fibers

Although there are now commercialized solutions for characterizing bulk thermoelectric materials, convenient testing methodologies for micron-scale thermoelectric fibers remain scarce. Shen *et al.*⁴⁵ introduced an *in situ* measurement for single thermoelectric fibers, enabling simultaneous acquisition of all three critical parameters—electrical conductivity, Seebeck coefficient, and thermal conductivity. This integrated approach delivers two strategic advantages. First, it eliminates errors in the microstructure of the samples. By avoiding segmented measurements of samples, it prevents errors in ZT calculations due to inherent structural differences in the fibers. Additionally, since the ZT value is inherently dimensionless, the methodology bypasses dimensional measurement uncertainties.

The *in situ* integrated characterization is based on the 3ω detection technique for micron-scale thermoelectric fibers. The electrical conductivity of the fiber specimen is precisely determined via a four-probe method, as illustrated in Fig. 19. A current I_F is applied between electrodes #2 and #5, while a nanovoltmeter measures the voltage U_F across the fiber. The resistance R is detected

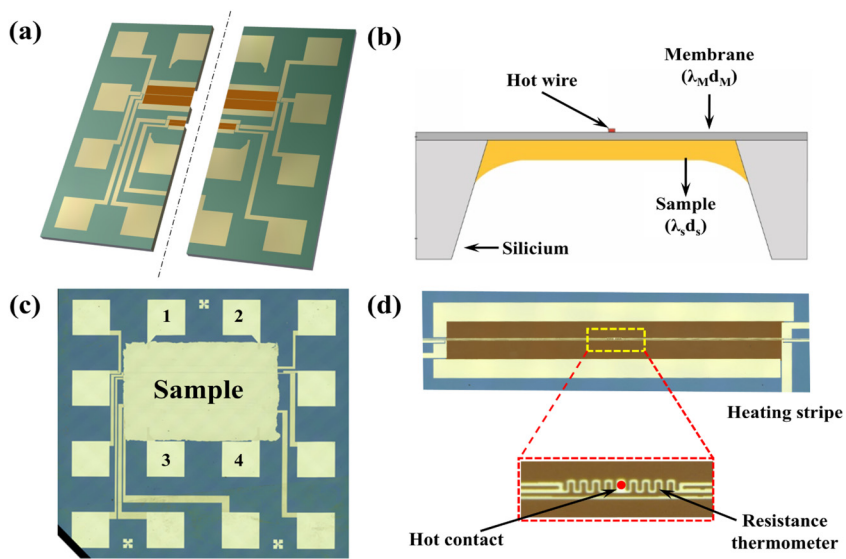


FIG. 18. (a) Van der Pauw chip. (b) Thermal conductivity by the 3ω method. (c) Electrical resistivity by the van der Pauw method. (d) Test structure for the Seebeck coefficient.

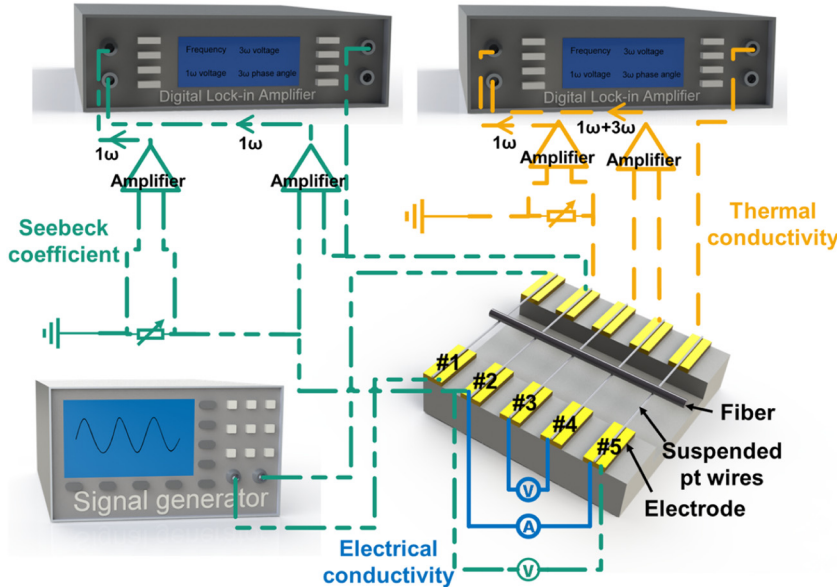


FIG. 19. The schematic diagram of the measurement system includes a digital lock-in amplifier, a signal generator, a detector, a variable resistor, and connecting circuits. The detector consists of a ceramic substrate, five pairs of electrodes, and a fiber sample suspended by five platinum wires. The blue solid line, green dashed line, and yellow dotted line represent the measurement circuits for electrical conductivity, Seebeck coefficient, and thermal conductivity, respectively.⁴⁵ Reproduced from Shen et al., Energy Mater. Adv. 5, 0124 (2024). Copyright (2024) AAAS Publishing.

06 December 2025 08:34:26

from Ohm's law, and conductivity is calculated as

$$\sigma = \frac{L_F I_F}{A_F U_F} = \frac{L_F}{A_F R}, \quad (37)$$

where L_F is the fiber length between voltage probes and A_F is the cross-sectional area.

The Seebeck coefficient is characterized by establishing a controlled temperature gradient along the sample fiber using a heated platinum wire #1. Platinum wire #1 maintains intimate thermal contact with the fiber while ensuring electrical isolation. A stable axial temperature gradient is induced via a precision current source. The Seebeck voltage between #2 and #5 is measured with a nanovoltmeter. The temperature difference is measured by using the linear resistance-temperature relationship of platinum,

$$S = \frac{\Delta V}{\Delta T} = \frac{V_5 - V_2}{R_2/R'_2 - 1 - R_5/R'_5 - 1} = \frac{\Delta V_{52}}{V_2/V'_2 - 1} = \frac{\Delta V_{52} V'_2 \alpha_R}{V_2 - V'_2}, \quad (38)$$

where α_R is the temperature coefficient of resistance. R_2 , R'_2 , R_5 , and R'_5 are resistances of Pt wires before and after heating, respectively. V_2 , V'_2 , V_5 , and V'_5 are voltage of Pt wires before and after heating, respectively. ΔV_{52} is the Seebeck voltage of samples generated by the temperature gradient.

Thermal conductivity measurements employ the 3ω technique, using the one-dimensional heat conduction model established by Lu et al.³⁰ Within this framework, thermal conductivity is derived from the 3ω voltage response as

$$V_{3\omega} = \frac{4I_\omega^3 R R' L_F}{\lambda \pi^4 A_F \sqrt{1 + (2\omega\gamma)^2}}, \quad (39)$$

where $V_{3\omega}$, I_ω , λ , and γ represent 3ω voltage, ω current, thermal conductivity, characteristic time constant. L_F and A_F are fiber length and cross-sectional area, respectively. After introducing a small amount of error into the approximate solution, the formula can be simplified to the following expression: $\tan \phi \approx 2\omega\gamma$, where ϕ is a phase angle of 3ω . Therefore, the final thermal conductivity of the one-dimensional thermoelectric sample can be calculated by the following formula:

$$\lambda = \frac{4V_\omega^3 R' L_F}{\pi^4 V_{3\omega} A_F R^2 \sqrt{1 + \tan^2 \phi}}. \quad (40)$$

The measurement process is as follows: First, the resistance of the resistance box is precisely adjusted to be equal to the resistance of the sample fiber measured by the digital lock-in amplifier in the A-B mode. Next, the filtering function of the digital lock-in amplifier needs to be turned off, and the low-frequency DC mode is selected to ensure the accuracy of signal detection. After the vacuum chamber and the detector temperature reach a stable state, the 1ω voltage, 3ω voltage, and 3ω phase angle data collected by the A port and B port of the digital lock-in amplifier at different frequencies are recorded. During this process, $0 < \omega\gamma < 4$ needs to be maintained to ensure the stability of the voltage and phase signals. Theoretically, the curve of the 3ω voltage $V_{3\omega}$ and the phase angle $\tan \phi$ changing with frequency should meet the boundary conditions of the measurement (the functional relationship between the parameters). Subsequently, by adjusting the input voltage, it is further verified whether the 3ω voltage has a linear relationship with the cube of the current at a fixed frequency. Additionally, it is important to ensure that the current value is neither too large nor too small, given the limitations of the measurement conditions, radiative heat loss, and the relatively weak 3ω voltage signal.

Critically, this *in situ* method directly computes the dimensionless thermoelectric figure of merit ZT independent of geometric parameters, thereby eliminating dimensional measurement uncertainties inherent in conventional approaches. The measurement results are shown in Fig. 20. The precision of *in situ* characterization testing also depends on the uniformity of the material and good electrical contact,

$$ZT = \frac{S^2 \sigma T}{\lambda} = \frac{\pi^4 TV_{3\omega} R \sqrt{1 + \tan \phi^2 (\Delta V_{52} V'_2 \alpha_R)^2}}{4V_0^3 R' (V_2 - V'_2)^2}. \quad (41)$$

D. Applications of the 3ω method in other fields

1. Thermal contact resistance

The 3ω method not only enables efficient and rapid measurement of thermal conductivity across various materials, but also stands out for its unique approach to testing other parameters such as thermal contact resistance. Testing thermal contact resistance between materials presents considerable challenges.⁴⁶ The 3ω method is a significant technique for detecting contact thermal resistance between thin films and substrates. In 1996, Lee and Cahill⁴⁷ employed the 3ω method to investigate the influence of interfacial thermal resistance on the out-of-plane thermal conductivity of SiO_2 and SiN_x dielectric films with varying thicknesses. During measurement, a metal-heating/sensing wire is deposited on the dielectric film. By applying an alternating current for heating, the relationship between the temperature oscillation amplitude and frequency is analyzed to derive the thermal resistance. For thin-film samples, the total temperature oscillation ΔT can be decomposed into the response ΔT_{Si} of the silicon substrate and the additional temperature rise ΔT_f of the film layer and interface,

$$\Delta T = \Delta T_f + \Delta T_{\text{Si}}, \quad (42)$$

$$\Delta T_{\text{Si}} = \frac{P}{l\pi\Lambda_{\text{Si}}} \left[\frac{1}{2} \ln \left(\frac{\Lambda_{\text{Si}}}{C_{\text{Si}} \left(\frac{w}{2} \right)^2} \right) + \eta - \frac{1}{2} \ln (2\omega) \right], \quad (43)$$

$$\Delta T_f = \frac{P}{\Lambda_a w} t, \quad (44)$$

$$\Lambda_a = \frac{\Lambda_i}{1 + R_I \Lambda_i / t}, \quad (45)$$

$$R_f = R_I + \frac{t}{\Lambda_i}. \quad (46)$$

In the formula, Λ_{Si} denotes the thermal conductivity of the Si substrate, C_{Si} represents its heat capacity, l and w denote the length and width of the heater, respectively. t is the thickness of the dielectric film, Λ_a is the apparent thermal conductivity, Λ_i is the intrinsic thermal conductivity of the film, and R_I is the interfacial thermal resistance. Based on the principle of thermal resistance superposition, when an interfacial thermal resistance R_I exists, the relationship between the apparent thermal conductivity Λ_a and the

intrinsic thermal conductivity Λ_i of the film is shown in Eq. (4). By fitting the properties of samples with different thicknesses, the interfacial thermal resistance R_I can be deduced. The results indicate that when the film thickness is less than 50 nm, its thermal conductivity decreases significantly with thickness reduction. This decrease is independent of temperature and primarily attributed to the additional effect of interfacial thermal resistance, which at room temperature is approximately 2×10^{-8} K m²/W—equivalent to a 20 nm thick SiO_2 layer. In 2019, Deng *et al.*⁴⁸ similarly employed the 3ω method to measure the interfacial thermal resistance of 4H-SiC/ SiO_2 . As shown in Fig. 21, linear fitting of the relationship between film thickness and total thermal resistance yielded an interfacial thermal resistance of 8.11×10^{-8} m²K/W at 298 K for the SiC/ SiO_2 interface, approximately four times that of the Si/ SiO_2 interface.

Wang *et al.*⁴⁹ measured the interfacial thermal resistance between SiO_2 -GaN films and sapphire substrates over the temperature range of 260–480 K using the 3ω method, with the measurement setup illustrated in Fig. 22. The entire measurement was conducted under a vacuum of 2.5×10^{-7} mbar, where Joule heating was generated by applying an alternating current to the heater. The resistance of the heater was matched by adjusting a series resistor to suppress the 1ω signal in the 3ω signal. Two operational amplifiers were used to measure the differential voltages across the heater and potentiometer, respectively. The 1ω and 3ω voltages were measured by a phase-locked amplifier, with the frequency measured up to 30 kHz. At room temperature, the contact thermal resistance of GaN film/sapphire was 1.02×10^{-7} m²K W⁻¹ and increased with rising temperature; the contact thermal resistance of SiO_2 /GaN was $\sim 7.76 \times 10^{-8}$ m²K W⁻¹ at room temperature and decreased with increasing temperature.

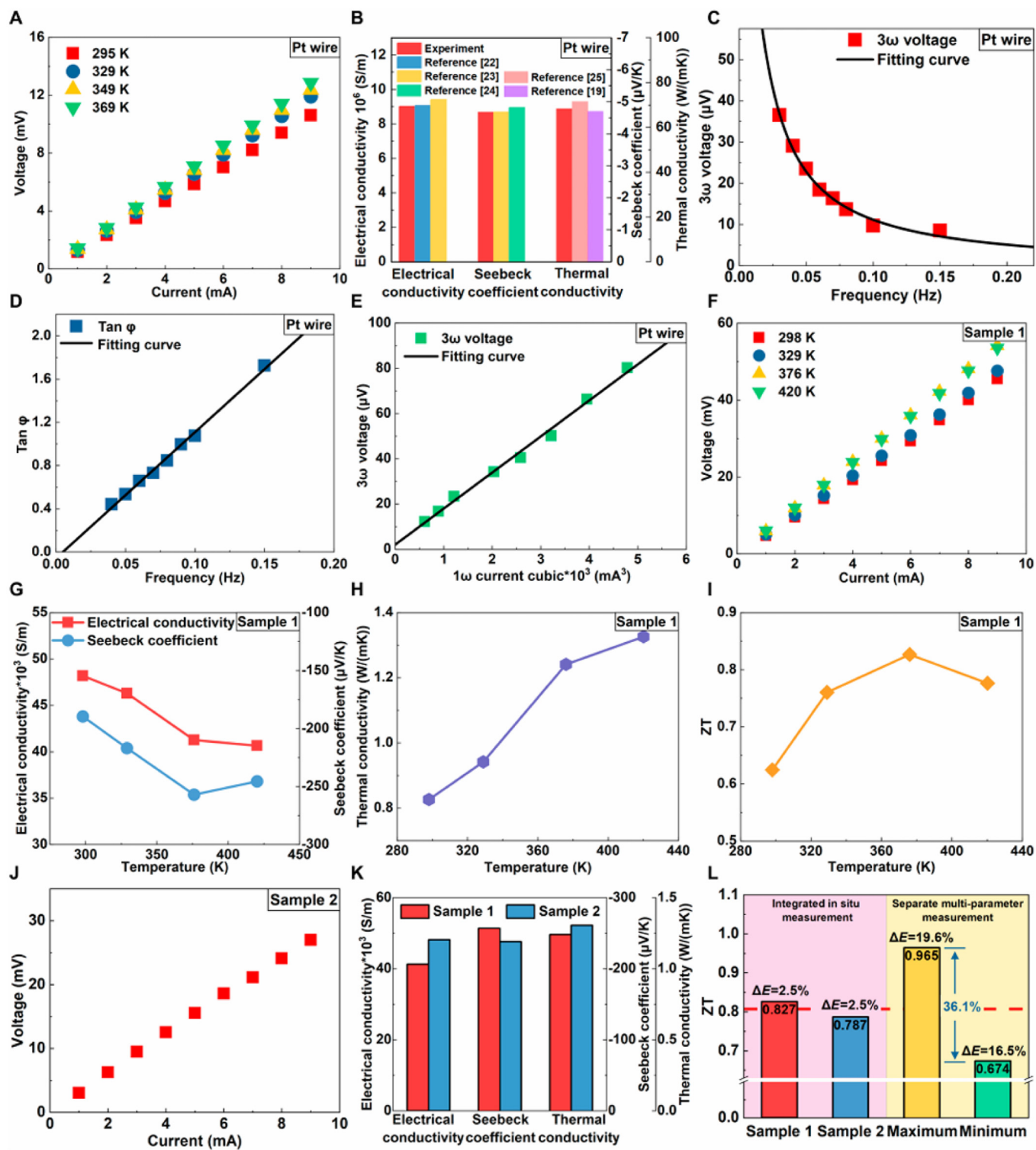
The overall equivalent thermal resistance model $Z(\omega)$ for a multilayer structure is as follows:

$$Z(\omega) = R_{c1} + R_{c2} + \left[\left(\left(-e\sqrt{i2\omega} \right)^{-1} + R_{\text{GaN}} \right)^{-1} + i\omega C_{\text{GaN}} \right]^{-1}, \quad (47)$$

$$Z_m(\omega) = -\frac{2R_0 bl}{\alpha_{\text{CR}} V_{1\omega}^3} V_{3\omega}. \quad (48)$$

In the formula, e represents the thermal effusivity of the substrate, R_{GaN} denotes the thermal resistance of GaN, C_{GaN} signifies the heat capacity of GaN, R_0 and α_{CR} denote the resistance and temperature coefficient of the metal heater, respectively. $V_{1\omega}$ and $V_{3\omega}$ represent the applied voltage and the 3ω voltage measured via the phase-locked amplifier, respectively.

However, Hua and Cao⁵⁰ pointed out that the traditional 3ω method for measuring interfacial thermal resistance has the following shortcomings: the two-dimensional thermal conduction model does not align with reality; the simplified series thermal resistance model introduces significant errors; and the actual thermal conductivity of the substrate is not measured. Furthermore, the heater must be sufficiently wide to satisfy the assumption of series thermal resistance combinations for different components. Yet,



06 December 2025 08:34:26

FIG. 20. Measurement results of thermoelectric fibers using the 3 ω method.⁴⁵ Reproduced from Shen et al., Energy Mater. Adv. 5, 0124 (2024). Copyright (2024) AAAS Publishing.

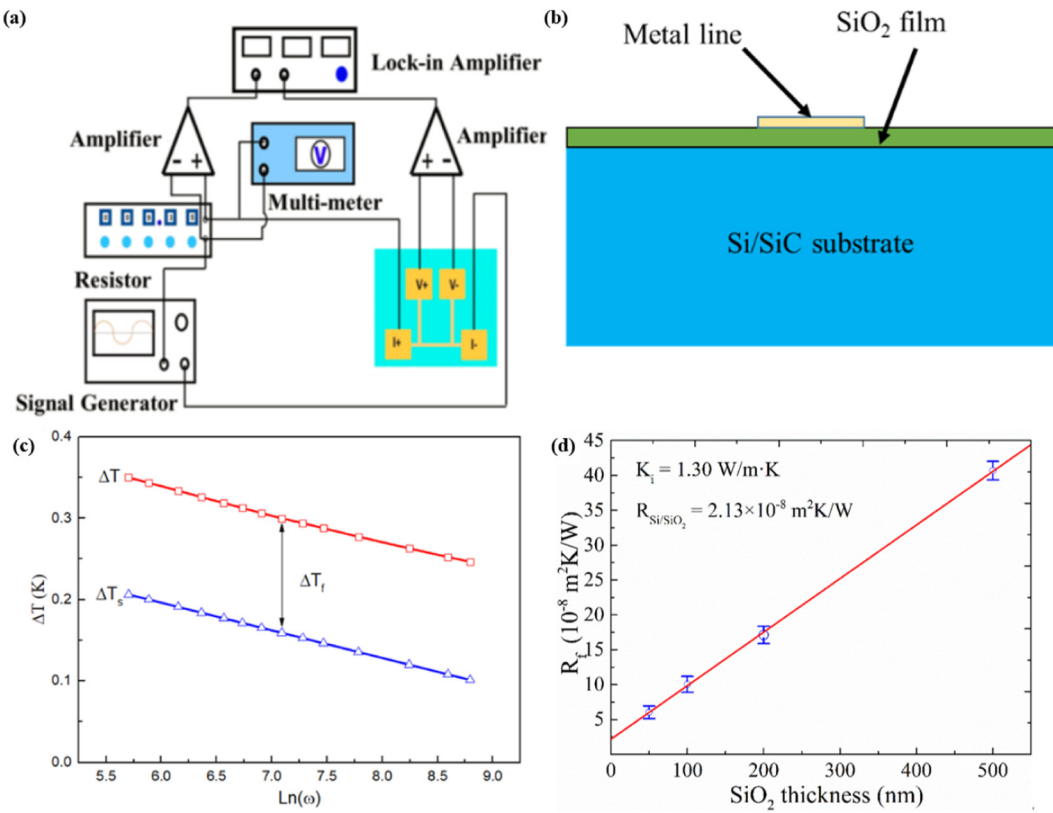


FIG. 21. (a) The schematic diagram of the 3ω setup. (b) The sketch graph of the experimental model. (c) Temperature oscillation vs logarithm angular frequency. (d) Apparent thermal resistance of SiO_2 thin films on the Si substrate.⁴⁸ Reproduced from Deng *et al.*, Appl. Phys. Lett. **115**(10), 101603 (2019). Copyright (2019) AIP Publishing LLC.

06 December 2025 08:34:26

increasing the heater width exacerbates errors in interfacial thermal resistance caused by uncertainties in estimating the substrate thermal conductivity. These issues contribute to substantial measurement errors in boundary thermal resistance. Building upon

this, Hua *et al.* proposed a dual-sensor 3ω - 2ω method, as illustrated in Fig. 23. This approach employs two metal sensors of different widths to measure interfacial thermal resistance through a three-step process. First, the 3ω method applies an AC current to

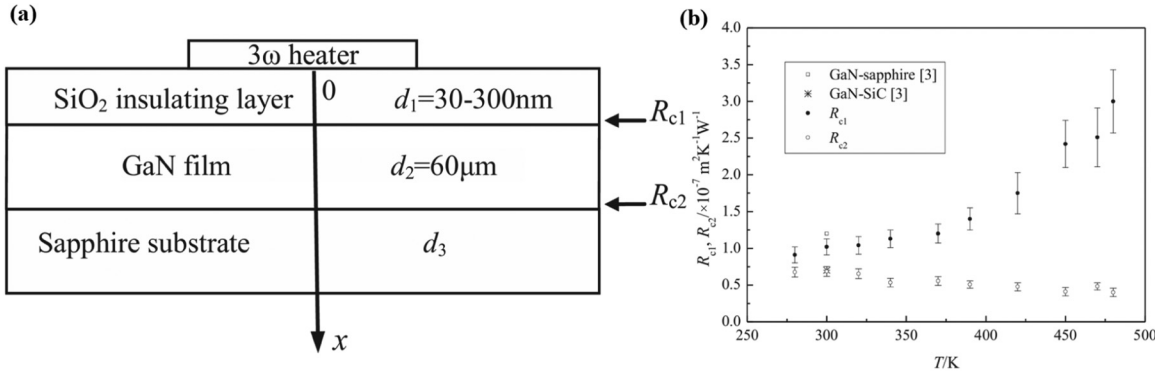


FIG. 22. (a) Schematic diagram of the 3ω method for measuring interfacial thermal resistance by Wang *et al.* (b) Thermal boundary resistance as a function temperature for SiO_2/GaN and $\text{GaN}/\text{sapphire}$ interfaces.⁴⁹ Reproduced from Wang *et al.*, Int. J. Therm. Sci. **87**, 178–186 (2015). Copyright (2015) Elsevier Ltd.

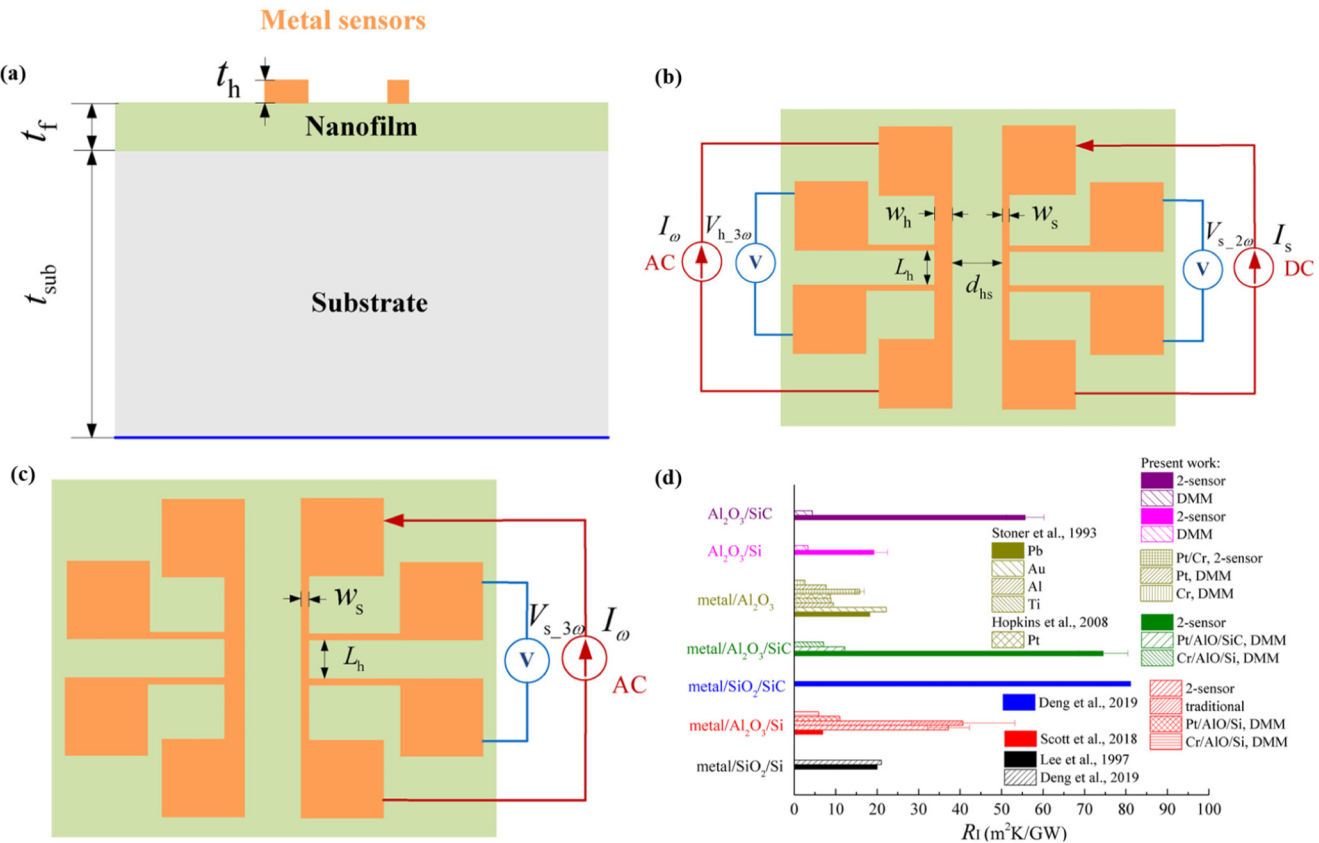


FIG. 23. (a)–(c) Schematic diagram of the dual-sensor 3ω - 2ω method. (d) Comparisons of TBRs between present data, DMM-based predictions, and previous measurements.⁵⁰ Reproduced from Hua and Cao, J. Appl. Phys. **129**(12), 125107 (2021). Copyright (2021) AIP Publishing LLC.

06 December 2025 08:34:26

the wide sensor to measure the film thermal conductivity k_f . Next, the 2ω method heats the wide sensor while the narrow sensor measures temperature, fitting the substrate thermal conductivity k_s . Finally, the 3ω method uses self-heating temperature measurement from the narrow sensor to infer the interfacial thermal resistance by combining data from the previous two steps.

Compared to conventional methods, the dual-sensor 3ω - 2ω approach yields more precise results. Furthermore, when measuring different materials, the geometric parameters of the wide sensors must be redesigned to maintain measurement accuracy. Whether using the traditional 3ω method to measure interfacial thermal resistance or the 3ω - 2ω method to measure thermal resistance, it is essential to ensure the sensor is sufficiently wide to guarantee the validity of the one-dimensional heat transfer model when measuring the thermal conductivity of thin films.

In addition to measuring the interfacial thermal resistance between membrane materials, the 3ω method can also be used to measure the interfacial thermal resistance between fibers. The T-type 3ω method is suitable for measuring the contact thermal resistance of fibers at the microscale, offering advantages such as low uncertainty and ease of operation. In 2010, Wang *et al.*⁵¹

successfully measured the contact thermal resistance between two fibers using the T-type 3ω method. The T-type probe structure consists of a platinum wire heating element and a thicker test fiber, as shown in Fig. 24(a). The heating wire serves both as a heater and a thermometer; by applying an alternating current, the third harmonic voltage is measured to determine the temperature rise. The test fiber is pressed against the midpoint of the heating wire with a small displacement to form a bare contact interface. The interfacial thermal resistance comprises macroscopic and microscopic components. The macroscopic resistance R_{mac} is obtained by integrating the elliptical contact model, reflecting overall geometry and thermal conductivity characteristics. The microscopic resistance R_{mic} correlates with surface roughness and material hardness,

$$R_j = \frac{1}{\pi \lambda_m a} \int_0^{\frac{\pi}{2}} \frac{1}{\sqrt{1 - \psi^2 \sin^2 \tau}} d\tau + \frac{\sigma}{\xi \lambda_m S_c} \left(\frac{F}{S_c H} \right)^{-\xi}. \quad (49)$$

In the formula, λ_m is the harmonic mean thermal conductivity, $\psi^2 = 1 - (b/a)^2$, $\sin \tau = a/\sqrt{a^2 + \eta}$, where a, b represent the contact areas of the semi-major and semi-minor axes, respectively,

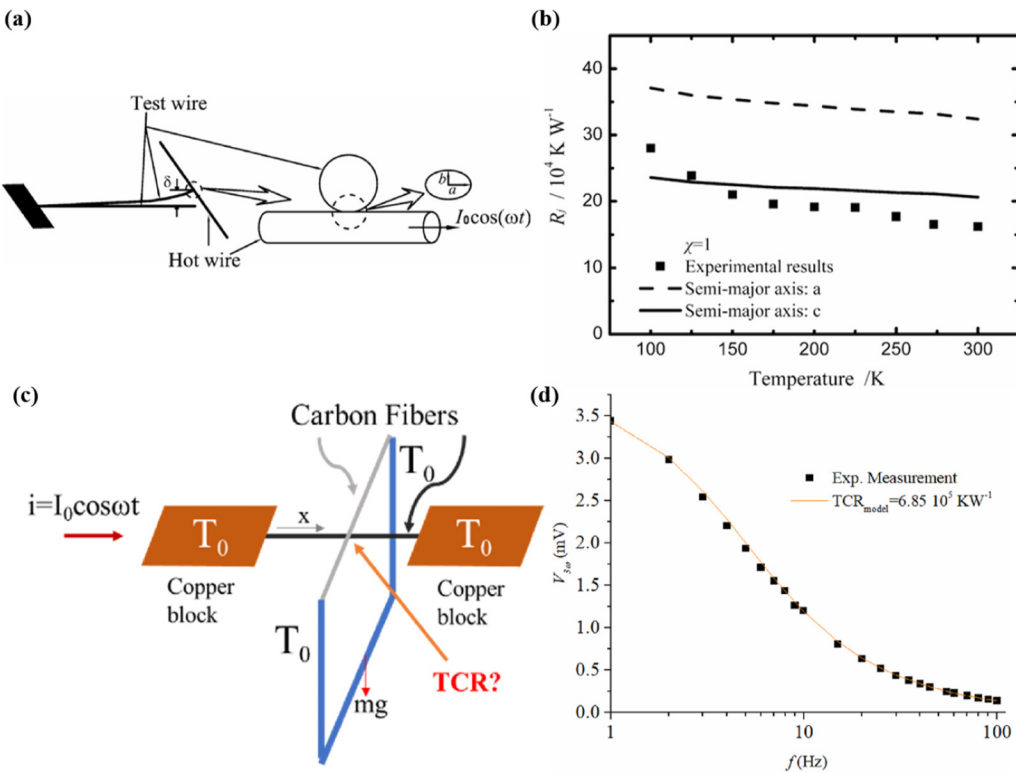


FIG. 24. (a) Schematic diagram of the T-type 3ω method for measuring fiber contact thermal resistance. (b) Comparison of the experimental thermal resistance of the joint with theoretical predicted value.⁵¹ Reproduced from Wang *et al.*, Int. J. Heat Mass Transfer **53**(23–24), 5350–5354 (2010). Copyright (2010) Elsevier Ltd. (c) Intersecting carbon fibers TCR measurement using the T-type 3ω method. (d) Measured and computed $V_{3\omega}$ voltages after the estimation of TCR.⁵² Reproduced from Rodrigo and Garnier, Int. J. Therm. Sci. **193**, 108510 (2023). Copyright (2023) Elsevier Ltd.

06 December 2025 08:34:26

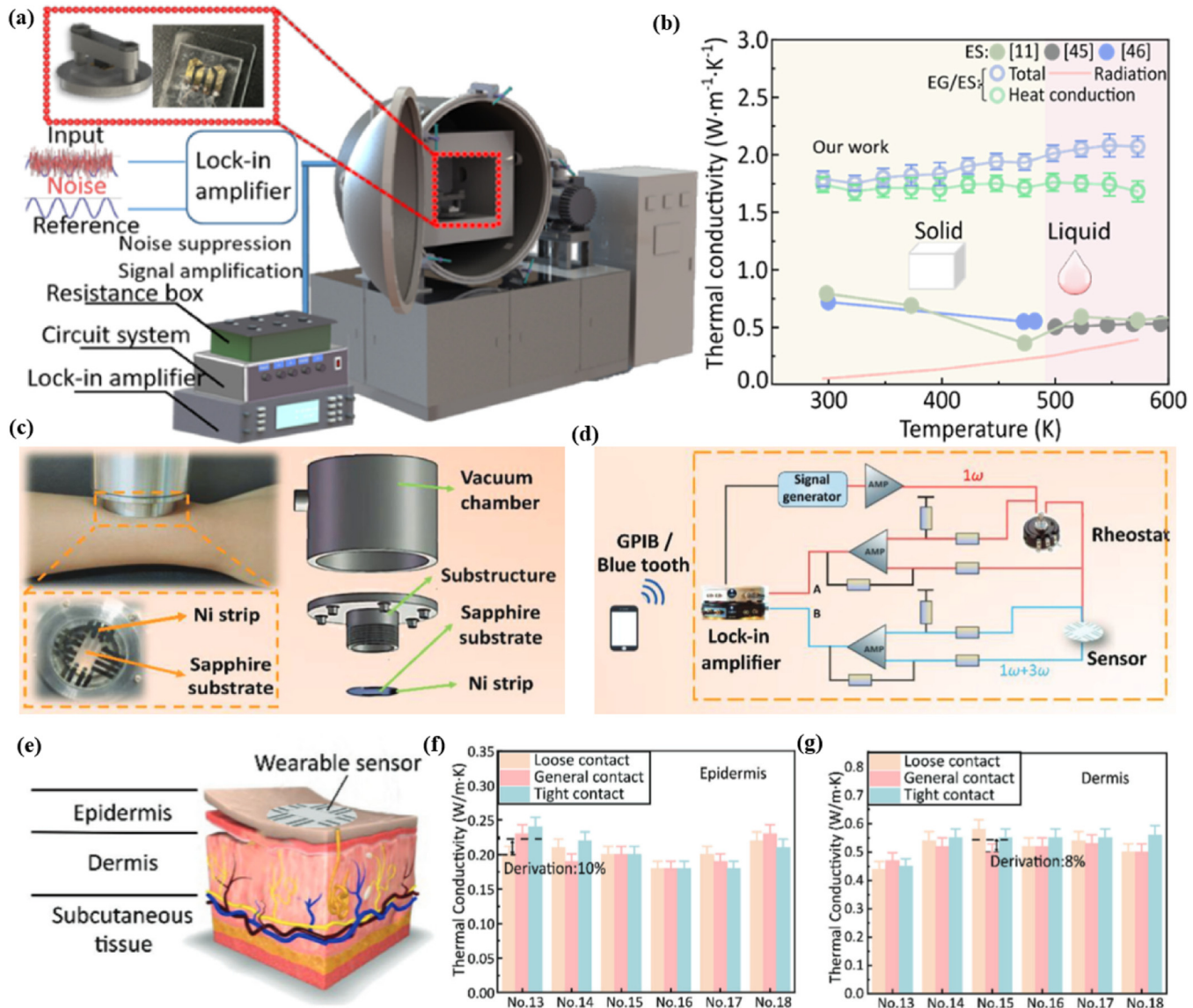
and η denotes the ellipsoidal coordinate. S_c is the macroscopic contact area, σ is the standard deviation of surface height, H is the material hardness, ξ is the conductivity-load index, and F is the contact load. The entire testing process was conducted in a vacuum environment (10^{-3} Pa). First, the thermal properties of the heating wire were calibrated using the 3ω method. Subsequently, the third harmonic voltage variation was measured during the connection state to calculate the total interfacial thermal resistance R_j . In addition, Wang *et al.*⁸ also achieved simultaneous measurement of the thermal conductivity of a single fiber and quantitative extraction of the contact thermal resistance at the fiber-probe interface. This approach was validated using Pt wires. Results indicated an interfacial thermal resistance of 3.2×10^3 – $1.06 \times 10^4 \text{ K W}^{-1}$ for pure Pt wire interfaces, with an uncertainty of approximately 10%, validating the method's reliability. The contact thermal resistance at carbon fiber metal interfaces was approximately $(4.7\text{--}8.3) \times 10^3 \text{ K W}^{-1}$.

In 2023, Rodrigo and Garnier⁵² employed the T-type 3ω method to measure the contact thermal resistance between two intersecting carbon fibers, yielding $(10.4 \pm 10.1) \times 10^5 \text{ K W}^{-1}$. The measurement schematic is illustrated in Fig. 24(c). The carbon fibers were supported by two copper blocks. One fiber was

connected to a U-shaped sample holder via silver paste and contacted the other fiber, with silver paste applied to ensure good electrical contact between them. During measurement, current was applied to the first fiber to provide Joule heating. With only one fiber, its temperature distribution exhibits a sinusoidal pattern due to boundary conditions. When the second fiber contacts the first, the temperature distribution of the first fiber changes, lowering its average temperature along the fiber and thereby reducing its resistance. Using the 3ω method, the 3ω voltage measured between the ends of the first fiber contains information about its average temperature. Based on finite element analysis, Rodrigo and Garnier also developed a model for calculating the voltage distribution across the fibers,

$$\tilde{T}(x) = \left\| \frac{2}{L} \sum_{n=0}^{\infty} \frac{P^*}{k_x \beta_n (\alpha^2 + \beta_n^2)} \sin(\beta_n x) \right\|. \quad (50)$$

In the above formula, P^* represents the thermal power generated by the Joule effect, L and k_x denote the fiber length and axial thermal conductivity, respectively, $\alpha^2 = \frac{\rho C_p \omega i}{k_x}$, and $\beta_n = (n + 0.5) \frac{\pi}{L}$.



06 December 2025 08:34:26

FIG. 25. (a) Upgraded three method-based high-temperature thermo-physical property measurement platform. (b) Evolution trend of the total thermal conductivity for 15 wt. % EG/ES and comparison with reported values for ES at different temperatures.⁵⁴ Reproduced from Yan *et al.*, Compos. Sci. Technol. **259**, 110957 (2025). Copyright (2025) Elsevier Ltd. (c) Photograph of a harmonic wave-driven wearable sensor. (d) Electrical circuit of the harmonic wave method. (e) Illustration of the conformal contact of a harmonic wave-driven wearable sensor with the skin. (f) The thermal conductivity of epidermis under different degrees of tightness. (g) The thermal conductivity of dermis under different degrees of tightness.⁵⁵ Reproduced from Qiu *et al.*, Adv. Mater. Technol. **9**, 2301997 (2024). Copyright (2024) Wiley-VCH.

The T-type 3ω method for measuring contact thermal resistance offers convenient operation and high repeatability. When using the T-type 3ω method to measure the contact thermal resistance between two fibers, accurate measurements of the fiber diameter, length, and contact area between the two fibers are essential to enhance testing precision. Furthermore, to avoid measurement errors caused by convective heat transfer,

relevant experiments must be conducted under high-vacuum conditions.

2. Materials in the relevant fields

Beyond macroscopic solids, powders, and liquids, as well as microscopic fibers, films, and nanotube materials, the 3ω method is

also applicable to testing in other fields owing to its superior structure and performance.⁵³ For phase-change composite (PCM) materials, the 3ω method can also be employed for measurement. Yan *et al.*⁵⁴ measured the thermal conductivity of expanded graphite/eutectic salt composite phase-change materials (PCMs) with an upgraded free-standing 3ω technique. The measurement platform is shown in Figs. 25(a) and 25(b). The results demonstrated that the thermal conductivity of phase-change materials before and after phase transition can be obtained using the 3ω method and the measurement apparatus with non-destructiveness and high accuracy. The 3ω method is also involved in the field of human health monitoring. Qiu *et al.*⁵⁵ developed a rigid and robust wearable sensor driven by the harmonic wave, which can be comfortably wrist-worn for a long time. It can extract both the thermal conductivities of epidermis and dermis of humans. A photograph of a harmonic wave-driven wearable sensor and electrical circuit of the harmonic wave method are shown in Figs. 25(c) and 25(d). It utilized and refined the 3ω method multi-layer model to resolve the thermal conductivity of different tissues in the superficial layers of human skin. Following testing of multiple groups using the 3ω method, it was summarized that epidermal thermal conductivity exhibits positive dependence on the body surface temperature and the water content.

III. CONCLUSIONS

In summary, this tutorial has introduced the wide applicability of the 3ω harmonic detection method for characterizing solids, liquids, powders, gases, fibers, and film materials. The content focuses on the key issues and precautions that need to consider when applying the 3ω method to measure various materials. The application of commercial instruments and the expansion of other fields, such as *in situ* characterization of thermoelectric properties, have also been summarized. The purpose of this tutorial is to introduce the 3ω method and provide practical guidance and suggestions for experimental researchers.

The 3ω method holds immense potential for future development, primarily in the following directions. (1) Beyond macro- and micro-scale material measurements, the 3ω method can be extended into biomedical applications, such as measuring thermal conductivity in biological tissues. (2) Measurement systems are trending toward automation and integration, enhancing measurement efficiency and reliability. (3) Through technological refinements, the 3ω method is overcoming its traditional measurement limitations, enabling the expansion of the measurable temperature range to encompass both extreme high and low temperatures. (4) By integrating mathematical modeling with deep learning approaches, multiple thermal properties can be determined for complex structures, broadening the method's applicability. Despite its promising outlook, the 3ω method faces practical challenges in implementation, prompting ongoing development of targeted improvement strategies. (1) In actual devices, interfacial thermal resistance between electrode, thin films, and substrates, coupled with complex multilayer structures, complicates thermal field distributions. This introduces significant errors when relying on simplified analytical models. Numerical methods such as finite element analysis can precisely simulate three-dimensional heat transport in

complex real structures, investigate the impact of non-ideal factors, and establish more accurate parameter extraction methods. (2) The 3ω method relies on detecting minute third harmonic voltage signals. Environmental electromagnetic noise and inherent nonlinear distortion in signal amplifiers can degrade the signal-to-noise ratio, affecting measurement accuracy—particularly at high frequencies or under extreme temperatures. Optimizing electronic system architecture and refining system design may mitigate sensitivity to interference and enhance high-frequency performance. (3) Challenges in sample preparation for special scenarios and materials. For instance, testing is complicated by thermal resistance at ultra-thin film interfaces, while sample preparation for special materials and detector integration proves difficult. These issues necessitate the development of mathematical models combined with other testing methods, alongside the creation of specific sample preparation and measurement techniques.

Overall, the 3ω method holds great promise in the characterization of thermal properties in both macro-scale and micro/nano-scale materials due to its unique advantages. Future advancements through automated and integrated measurement systems, deeper integration with advanced numerical simulations, and continuous technological innovation addressing specific challenges are expected to enable the 3ω method to deliver more precise and convenient thermal property characterization solutions across a broader range of materials and under more extreme conditions.

ACKNOWLEDGMENTS

This work was supported by the National Key Research and Development Program of China (No. 2023YFB3809800), the National Natural Science Foundation of China (Nos. 52172249 and 52525601), the Scientific Instrument Developing Project of the Chinese Academy of Sciences (No. PTYQ2025TD0018), the Chinese Academy of Sciences Talents Program (No. E2290701), the Jiangsu Province Talents Program (No. JSSCRC2023545), the Special Fund Project of Carbon Peaking Carbon Neutrality Science and Technology Innovation of Jiangsu Province (No. BE2022011), and the Basic Research Program of Jiangsu Province (No. BK20251714).

AUTHOR DECLARATIONS

Conflict of Interest

The authors have no conflicts to disclose.

Author Contributions

X.Y. and H.Z. have contributed equally to this work.

Xiao Yang: Investigation (equal); Writing – original draft (equal).
Haibo Zhao: Investigation (equal); Writing – original draft (equal).
Chunyang Wang: Writing – review & editing (equal).
Yanan Shen: Writing – original draft (equal).
Zewen Song: Writing – original draft (equal).
Haisheng Chen: Project administration (equal); Writing – review & editing (equal).
Ting Zhang: Project administration (equal); Writing – review & editing (equal).
Xinghua Zheng: Project administration (equal); Writing – review & editing (equal).

DATA AVAILABILITY

The data that support the findings of this study are available from the corresponding authors upon reasonable request.

REFERENCES

- ¹X. Zheng, P. Yue, S. Li *et al.*, "Stethoscope-type 3ω independent detector for fast measurement of material thermal conductivity," *Rev. Sci. Instrum.* **89**(8), 084904 (2018).
- ²M. K. Samani, N. Khosravian, G. C. K. Chen *et al.*, "Thermal conductivity of individual multiwalled carbon nanotubes," *Int. J. Therm. Sci.* **62**, 40–43 (2012).
- ³M. K. Samani, X. Z. Ding, S. Amini *et al.*, "Thermal conductivity of titanium aluminum silicon nitride coatings deposited by lateral rotating cathode arc," *Thin Solid Films* **537**, 108–112 (2013).
- ⁴S. Chen, A. L. Moore, W. Cai *et al.*, "Raman measurements of thermal transport in suspended monolayer graphene of variable sizes in vacuum and gaseous environments," *ACS Nano* **5**(1), 321–328 (2011).
- ⁵D. H. Olson, J. L. Braun, and P. E. Hopkins, "Spatially resolved thermoreflectance techniques for thermal conductivity measurements from the nanoscale to the mesoscale," *J. Appl. Phys.* **126**(15), 150901 (2019).
- ⁶X. Qian, Z. Ding, J. Shin *et al.*, "Accurate measurement of in-plane thermal conductivity of layered materials without metal film transducer using frequency domain thermoreflectance," *Rev. Sci. Instrum.* **91**(6), 064903 (2020).
- ⁷W. Jang, W. Bao, L. Jing *et al.*, "Thermal conductivity of suspended few-layer graphene by a modified T-bridge method," *Appl. Phys. Lett.* **103**(13), 133102 (2013).
- ⁸J. L. Wang, M. Gu, X. Zhang *et al.*, "Thermal conductivity measurement of an individual fibre using a T type probe method," *J. Phys. D: Appl. Phys.* **42**(10), 105502 (2009).
- ⁹H. Wang, S. Hu, K. Takahashi *et al.*, "Experimental study of thermal rectification in suspended monolayer graphene," *Nat. Commun.* **8**(1), 1–8 (2017).
- ¹⁰D. G. Cahill, "Thermal conductivity measurement from 30 to 750 K: The 3ω method," *Rev. Sci. Instrum.* **61**(2), 802–808 (1990).
- ¹¹L. Qiu, Y. Ouyang, Y. Feng *et al.*, "Note: Thermal conductivity measurement of individual porous polyimide fibers using a modified wire-shape 3ω method," *Rev. Sci. Instrum.* **89**(9), 096112 (2018).
- ¹²P. Zhang, X. Ming, Y. Liu *et al.*, "An improved thermal conductivity measurement scheme for macroscopic graphitic films using the laser flash method," *J. Therm. Sci.* **33**(4), 1480–1490 (2024).
- ¹³Z. Wang, *Characterization of Thermal Properties and Thermal Transport Mechanisms of Micro Nano Scale Materials* (Graduate School of the Chinese Academy of Sciences, Beijing, 2007).
- ¹⁴T. Yamane, N. Nagai, S. Katayama *et al.*, "Measurement of thermal conductivity of silicon dioxide thin films using a 3ω method," *J. Appl. Phys.* **91**(12), 9772–9776 (2002).
- ¹⁵H. S. Carslaw and J. C. Jaeger, *Conduction of Heat in Solids* (Landon Oxford University Press, 1959), pp. 20–55.
- ¹⁶T. Borca-Tasciuc, D. Song, J. L. Liu *et al.*, "Anisotropic thermal conductivity of a Si/Ge superlattice," *Mater. Res. Soc.* **545**, 473–478 (1998).
- ¹⁷G. P. Su, X. H. Zheng, L. Qiu *et al.*, "Measurement of thermal conductivity of anisotropic SiC crystal," *Int. J. Thermophys.* **34**(12), 2334–2342 (2013).
- ¹⁸Y. S. Ju, K. Kurabayashi, and K. E. Goodson, "Thermal characterization of anisotropic thin dielectric films using harmonic Joule heating," *Thin Solid Films* **339**(1–2), 160–164 (1999).
- ¹⁹B. Yang, W. L. Liu, J. L. Liu *et al.*, "Measurements of anisotropic thermoelectric properties in superlattices," *Appl. Phys. Lett.* **81**(19), 3588–3590 (2002).
- ²⁰F. Chen, J. Shulman, Y. Xue *et al.*, "Thermal conductivity measurement under hydrostatic pressure using the 3ω method," *Rev. Sci. Instrum.* **75**(11), 4578–4584 (2004).
- ²¹D. H. Jung, T. W. Kwon, D. J. Bae *et al.*, "Fully automated dynamic calorimeter," *Meas. Sci. Technol.* **3**(5), 475–484 (1992).
- ²²N. O. Birge and S. R. Nagel, "Wide-frequency specific heat spectrometer," *Rev. Sci. Instrum.* **58**(8), 1464–1470 (1987).
- ²³Z. L. Wang, D. W. Tang, S. Liu *et al.*, "Thermal-conductivity and thermal-diffusivity measurements of nanofluids by 3ω method and mechanism analysis of heat transport," *Int. J. Thermophys.* **28**(4), 1255–1268 (2007).
- ²⁴E. Yusibani, P. L. Woodfield, M. Kohno *et al.*, "End effects in the three- ω method to measure gas thermal conductivity," *Int. J. Thermophys.* **30**(3), 833–850 (2009).
- ²⁵X. Zheng, L. Qiu, P. Yue *et al.*, "3 ω slope comparative method for fluid and powder thermal conductivity measurements," *Mod. Phys. Lett. B* **30**(25), 1650322 (2016).
- ²⁶D. G. Cahill, M. Katiyar, and J. R. Abelson, "Thermal conductivity of a-Si: H thin films," *Phys. Rev. B* **50**(9), 6077–6081 (1994).
- ²⁷B. W. Olson, S. Graham, and K. Chen, "A practical extension of the 3ω method to multilayer structures," *Rev. Sci. Instrum.* **76**(5), 053901 (2005).
- ²⁸T. Tong and A. Majumdar, "Reexamining the 3ω -omega technique for thin film thermal characterization," *Rev. Sci. Instrum.* **77**(10), 104902 (2006).
- ²⁹D. J. Yao, H. C. Chien, Y. C. Liu *et al.*, "The study of thin films thermal conductivity measurement by 3ω method," in *Proceedings of International Symposium on Nanotechnology and Energy, Hsinchu, Taiwan* (National Tsing Hua University, 2004).
- ³⁰L. Lu, W. Yi, and L. Zhang D, "3 ω method for specific heat and thermal conductivity measurements," *Rev. Sci. Instrum.* **72**(7), 2996–3003 (2001).
- ³¹X. Yang, H. Zhao, C. Wang *et al.*, "3 ω method for thermal conductivity measurement of thin sheet materials," *J. Appl. Phys.* **137**(17), 175102 (2025).
- ³²L. Qiu, Y. Ouyang, Y. Feng *et al.*, "Thermal conductivity measurements of individual porous polyimide fibers using a modified wire-shape 3ω method," *Rev. Sci. Instrum.* **89**(9), 096112 (2018).
- ³³L. Qiu, D. W. Tang, X. H. Zheng *et al.*, "The freestanding sensor-based 3ω technique for measuring thermal conductivity of solids: Principle and examination," *Rev. Sci. Instrum.* **82**(4), 045106 (2011).
- ³⁴X. Zheng, P. Yue, S. Li *et al.*, "Stethoscope-type 3ω independent detector for fast measurement of material thermal conductivity," *Rev. Sci. Instrum.* **89**(8), 084904 (2018).
- ³⁵T. Borca-Tasciuc, A. R. Kumar, and G. Chen, "Data reduction in 3ω method for thin-film thermal conductivity determination," *Rev. Sci. Instrum.* **72**(4), 2139–2147 (2001).
- ³⁶L. Qiu, X. H. Zheng, G. P. Su *et al.*, "Design and application of a freestanding sensor based on 3ω technique for thermal-conductivity measurement of solids, liquids, and nanopowders," *Int. J. Thermophys.* **34**(12), 2261–2275 (2013).
- ³⁷L. Qiu, X. Zheng, P. Yue *et al.*, "Adaptable thermal conductivity characterization of microporous membranes based on freestanding sensor-based 3ω technique," *Int. J. Therm. Sci.* **89**(3), 185–192 (2015).
- ³⁸L. Qiu, Y. Ma, Y. Ouyang *et al.*, "Freestanding flexible sensor based on 3ω technique for anisotropic thermal conductivity measurement of potassium dihydrogen phosphate crystal," *Sensors* **21**(23), 7968 (2021).
- ³⁹Q. Kong, L. Qiu, Y. D. Lim *et al.*, "Thermal conductivity characterization of three-dimensional carbon nanotube network using freestanding sensor-based 3ω technique," *Surf. Coat. Technol.* **345**, 105–112 (2018).
- ⁴⁰I. H. Tayman, "Effective thermal conductivity of isotropic polymer composites," *Int. Commun. Heat Mass Transfer* **25**(5), 723–732 (1998).
- ⁴¹D. Wang, C. Shen, J. Lan *et al.*, "Exploration of the correlation between weak absorption and thermal-stress for KDP and 70%-DKDP crystals," *J. Alloys Compd.* **790**, 212–220 (2019).
- ⁴²D. R. Lide, *CRC Handbook of Chemistry and Physics*, 81st ed. (CRC Press, Boca Raton, 2000).
- ⁴³B. W. Olson, S. Graham, and K. Chen, "A practical extension of the 3ω method to multilayer structures," *Rev. Sci. Instrum.* **76**(5), 053901 (2005).
- ⁴⁴Kaviany, *Principles of Heat Transfer in Porous Media* (Springer-Verlag, 1995).
- ⁴⁵Y. Shen, X. Yang, H. Zhao *et al.*, "In situ thermoelectric property characterization of microscale single thermoelectric fiber based on harmonic detection," *Energy Mater. Adv.* **5**, 0124 (2024).

- ⁴⁶Y. Wang, X. Sun, H. Kang *et al.*, “Thermal contact resistance and heat transfer enhancement mechanisms at non-smooth contact interfaces,” *J. Therm. Sci.* **34**(2), 465–497 (2025).
- ⁴⁷S. M. Lee and D. G. Cahill, “Heat transport in thin dielectric films,” *J. Appl. Phys.* **81**(6), 2590–2595 (1997).
- ⁴⁸S. Deng, C. Xiao, J. Yuan *et al.*, “Thermal boundary resistance measurement and analysis across SiC/SiO₂ interface,” *Appl. Phys. Lett.* **115**(10), 101603 (2019).
- ⁴⁹Z. L. Wang, G. Yao, M. Sun *et al.*, “Reconstruction of thermal boundary resistance and intrinsic thermal conductivity of SiO₂-GaN-sapphire structure and temperature dependence,” *Int. J. Therm. Sci.* **87**, 178–186 (2015).
- ⁵⁰Y. C. Hua and B. Y. Cao, “A two-sensor 3ω-2ω method for thermal boundary resistance measurement,” *J. Appl. Phys.* **129**(12), 125107 (2021).
- ⁵¹J. Wang, B. Song, M. Gu *et al.*, “Temperature dependence of thermal resistance of a bare joint,” *Int. J. Heat Mass Transfer* **53**(23–24), 5350–5354 (2010).
- ⁵²O. Rodrigo and B. Garnier, “Thermal contact resistance measurement between two intersecting PAN type carbon fibers using the T-type 3ω method,” *Int. J. Therm. Sci.* **193**, 108510 (2023).
- ⁵³Y. Ouyang, J. Lin, J. Pei *et al.*, “A harmonic-wave bio-thermal method for continuous monitoring skin thermal conductivity and capillary perfusion rate,” *Nano Res.* **17**, 4420–4427 (2024).
- ⁵⁴K. Yan, L. Qiu, H. Li *et al.*, “Expanded graphite encapsulation of nitrates for enhanced thermal transport: Mechanism insight and component screening,” *Compos. Sci. Technol.* **259**, 110957 (2025).
- ⁵⁵L. Qiu, X. Wang, Y. Ouyang *et al.*, “Non-invasive skin thermo-diagnosis based on a harmonic wave-driven wearable sensor,” *Adv. Mater. Technol.* **9**, 2301997 (2024).